APPLICATION OF L1 RECONSTRUCTION OF SPARSE SIGNALS TO AMBIGUITY RESOLUTION IN RADAR

A Thesis
Presented to
The Academic Faculty

by

Fahad Shaban

In Partial Fulfillment
of the Requirements for the Degree
M.S. ECE in the
School of Electrical and Computer Engineering

Georgia Institute of Technology
May, 2013

APPLICATION OF L1 RECONSTRUCTION OF SPARSE SIGNALS TO AMBIGUITY RESOLUTION IN RADAR

Approved by:

Dr. Mark A. Richards, Advisor
School of Electrical and Computer Engineering
Georgia Institute of Technology

Dr. Justin K. Romberg
School of Electrical and Computer Engineering
Georgia Institute of Technology

Dr. Aaron D Lanterman
School of Electrical and Computer Engineering
Georgia Institute of Technology

Date Approved: March 29, 2013

To my inspiring parents: Sanaullah and Razia, who taxed themselves for years to earn an honest living for my upbringing and education

ACKNOWLEDGEMENTS

I wish to express my deepest sense of gratitude and indebtedness to my advisor Dr. Mark A. Richards for his valuable guidance and insightful suggestions throughout the course of this project. He also took a lot of pain in going through the dissertation and making necessary corrections and suggesting improvements as and when required. I am also thankful to my friends who contributed to this project in large and small ways. I would like to offer special thanks to Dr. Justin Romberg and Dr. Aaron Lanterman who kindly agreed to serve on the reading committee for this Master's thesis.

TABLE OF CONTENTS

LIST OF TABLES

LIST OF FIGURES

SUMMARY

The objective of the proposed research is to develop a new algorithm for range and Doppler ambiguity resolution in radar detection data using L^1 minimization methods for sparse signals and to investigate the properties of such techniques. This novel approach to ambiguity resolution makes use of the sparse measurement structure of the post-detection data in multiple pulse repetition frequency radars and the resulting equivalence of the computationally intractable L^0 minimization and the surrogate L^1 minimization methods. The ambiguity resolution problem is cast as a linear system of equations which is then solved for the unique sparse solution in the absence of errors. It is shown that the new technique successfully resolves range and Doppler ambiguities and the recovery is exact in the ideal case of no errors in the system. The behavior of the technique is then investigated in the presence of real world data errors encountered in radar measurement and detection process. Examples of such errors include blind zone effects, collisions, false alarms and missed detections. It is shown that the mathematical model consisting of a linear system of equations developed for the ideal case can be adjusted to account for data errors. Empirical results show that the L^1 minimization approach also works well in the presence of errors with minor extensions to the algorithm. Several examples are presented to demonstrate the successful implementation of the new technique for range and Doppler ambiguity resolution in pulse Doppler radars.

CHAPTER 1

INTRODUCTION

A radar measurement process is designed to infer information about a target – a remotely located object of interest. The fundamental radar operation of measuring reflections off of the target from the transmitted electromagnetic energy is followed by various processing steps to measure quantities such as range, speed and angular position of the target. Pulsed radars operate by transmitting a succession of short pulses of electromagnetic energy. The range to the target is measured by estimating the round trip return timing of the transmitted signal, but it can be difficult to distinguish returns from the target and other unwanted objects located at the same distance. In case of moving targets, the use of Doppler processing allows measurement of another characteristic of the echo signal – the Doppler shift with respect to the transmitted signal, which can be used to measure the range rate or speed of the target. The characteristics of the pulsed radar signal largely determine the performance and capability of the radar. Pulse power, pulse repetition rate, pulse width and modulation are traded off to obtain the optimum combination for a given application. Pulse power and width directly affect the maximum distance, or range, of a target that can be detected by the radar. Pulse width also determines the range resolution in pulsed radars. Since modern radars rely heavily on digital signal processing carried out on the raw data collected from the echo signals, we will first describe the range and Doppler measurement process and the sampling requirements for each of the two measurements.

Measurement of Range and Doppler in Pulse Doppler Radars

Pulse Doppler radars estimate the range and radial velocity of multiple targets in the radar's field of view with the help of two time sampling intervals. The radar emits a periodic series

of pulses at a rate which constitutes one of the sampling intervals. The time between pulses T is commonly called the *pulse repetition interval* (*PRI*) or *inter-pulse period* (*IPP*), and the corresponding frequency $1/T$ is called the *pulse repetition frequency* (*PRF*). The PRF typically ranges from a few hundred hertz to a few hundreds of kilohertz. In a portion of the time period between pulses the received signal is sampled at a high rate, typically in the range of hundreds of kilohertz to a few tens of megahertz. These are known as *fast-time* samples, and the cluster of high rate samples so obtained constitutes one column of the data matrix shown in Fig. 1.1. The cluster of samples from the next pulse is stored in the next column and so forth. The fast time sampling interval T_s between successive samples of the echoes of a single pulse is the interval between radar measurements occupying successive rows of the data matrix, and it determines the spacing of the radar range samples called the *range bins*. The range bin spacing is then given by $R_{ua} = c \cdot T_s/2$ meters, where c is the speed of light (about 3×10^8 m/s). The horizontal dimension in Fig. 1.1 constitutes the *slow-time* samples separated by the pulse repetition interval T mentioned earlier.

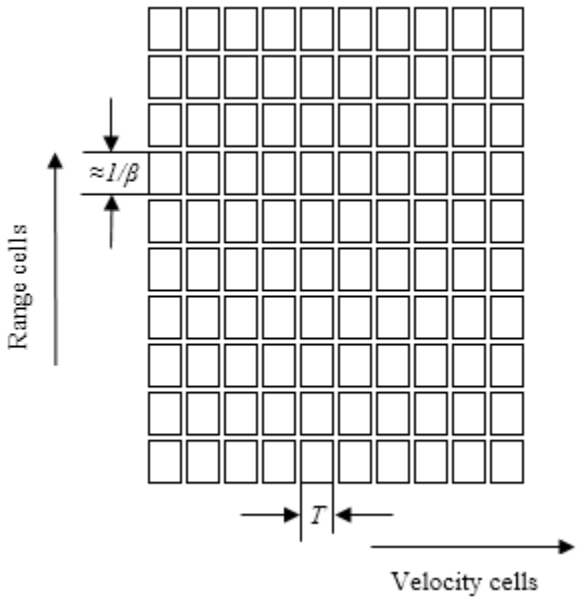

Fig. 1.1 Fast time/slow-time data matrix.

The fast-time sampling interval is chosen based on the Nyquist sampling criterion which states that the sampling rate should equal or exceed the bandwidth of the received signal. In radars, the bandwidth of the received fast-time signal is limited by the bandwidth of the transmitted pulse. Assuming a simple constant frequency pulse, the spectrum is a sinc function in the frequency domain. The spectrum of the time-limited simple pulse with pulse width τ has an infinite support in the frequency domain, meaning that it is not band-limited. However, the Rayleigh bandwidth of the simple pulse (4-dB down) is $1/\tau$ Hz which serves as a good approximate bandwidth measure [1]. The Nyquist sampling interval in fast time is then simply given by $1/\tau$ seconds.

The slow-time sampling interval is simply the pulse repetition interval *T* and this is the interval between radar measurements occupying the same row in successive columns of the data matrix. When there is relative motion from one pulse to the next between the radar and the scatterer, the phase of the return echoes from successive pulses will vary from one slow-time sample to the next. This means that the slow time signal consisting of one row of the data matrix has a non-zero Doppler bandwidth, either due to the target motion or a moving radar platform. For this reason, the frequency spectrum of the slow time signal is also referred to as the Doppler spectrum. In order to carry out Doppler processing in the frequency domain, the Doppler spectrum of each row in the data matrix of Fig. 1.1 is first computed using the discrete Fourier transform (DFT), as shown in Fig. 1.2, prior to subsequent processing steps such as pulse Doppler target detection [1]. This operation transforms the fast-time/slow-time matrix to range-Doppler matrix.

Figure 1.3 shows the periodic train of simple pulses in time domain, while its spectral representation is shown in Fig. 1.4. The frequency response is composed of discrete spectral lines spaced at an interval equal to PRF and weighted by the envelope of the frequency spectrum of the single pulse.

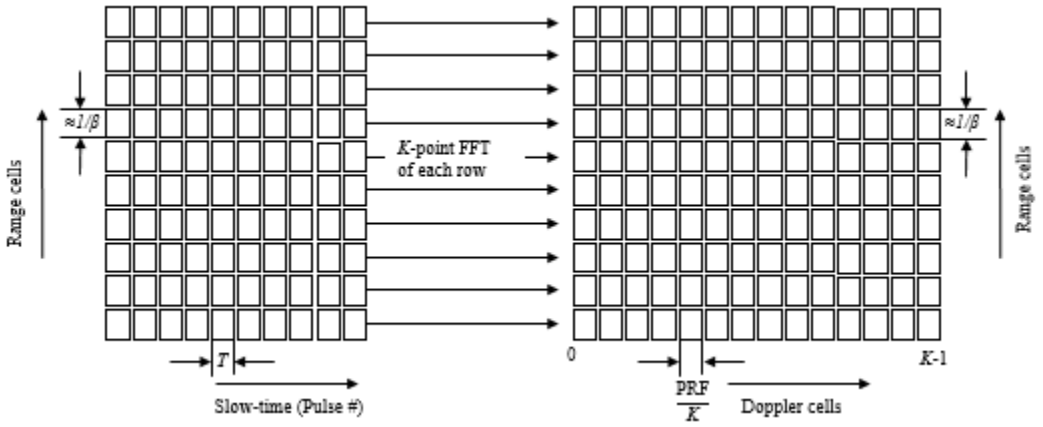

Fig. 1.2 Range-Doppler matrix.

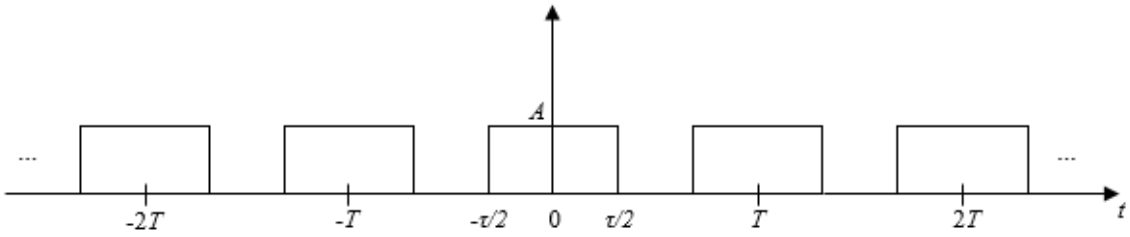

Fig. 1.3 Pulse train with infinite support in time domain.

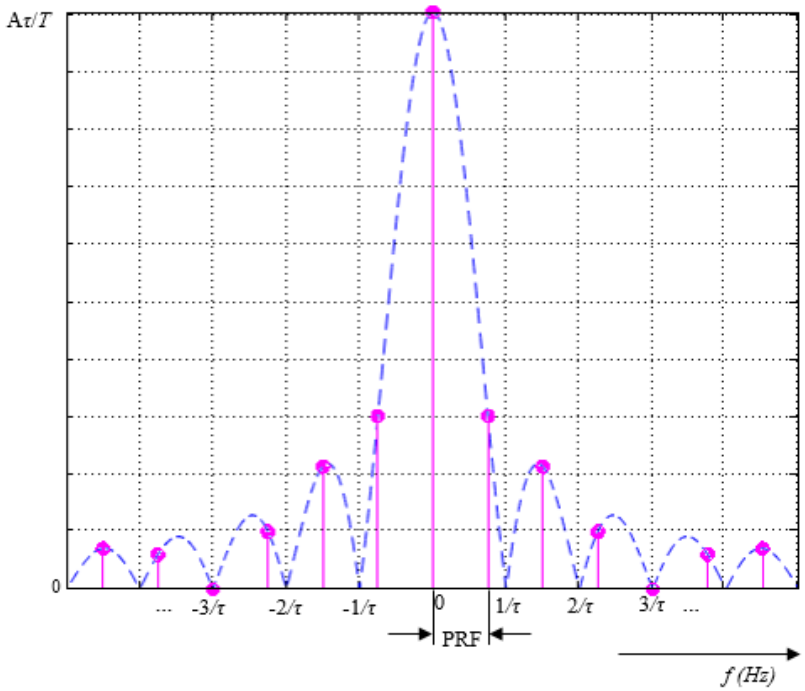

Fig. 1.4 Spectrum of infinite pulse train.

The train of simple pulses transmitted by the radar, however, is always time-limited. A finite pulse train of M_p pulses can be modeled as an infinite train of simple pulses multiplied by a longer simple pulse as shown in Fig. 1.5. In this case, the only change in the spectrum from Fig. 1.4 is that the impulsive spectral lines are replaced by narrow sinc functions representing the Fourier transform of the longer simple pulse of duration $T_d=M_pT$ seconds, but still separated by an interval equal to the PRF $1/T$. The Rayleigh bandwidth of these short sinc pulses is given by $1/M_pT$ Hz which determines the resolution of the Doppler spectrum. The spectrum resolution therefore depends on the number of pulses in one row of the data matrix M and the pulse repetition interval T.

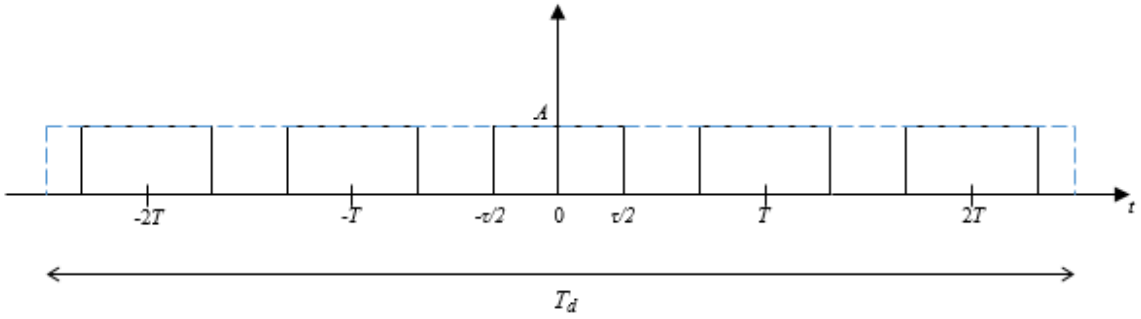

Fig. 1.5 Pulse train bounded in time.

As stated earlier, the frequency spectrum of M_p pulses is obtained by using a K-point DFT. The Nyquist sampling requirement in the frequency domain can be determined by taking the inverse DFT of the Doppler spectrum, which gives replicated samples of the time domain signal periodically spaced at an interval K. If $K \geq M_p$ the original slow-time signal can be recovered without aliasing after the DFT operation in the frequency domain. It must be noted, however, that the goal in radars is to infer information about the target, not to reconstruct the original signal from its samples. Thus, aliasing may be allowed in both range and Doppler measurements in pulse Doppler radars as we will see next in the discussion of range and Doppler ambiguities.

Range and Doppler Ambiguities

As stated earlier, a benefit of transmission of a pulsed signal is an increase in the detection capability of far-range targets. However, this advantage is coupled with the disadvantage of target range ambiguity. The measurements are, in fact, subject to aliasing ambiguities in both range and Doppler, making it difficult to determine the correct, unaliased range and Doppler shift of detected targets [2].

In radar signal processing, range ambiguities occur when received signals from different ranges appear to have the same range. As an example, range ambiguities can exist when a second pulse is transmitted before the most distant detectable echo from a previous pulse has been received. When that echo is received and detected, the processor does not know if it represents a target from the most recent pulse and a relatively short range, or the earlier pulse and a longer range. The apparent range R_a of the detected target becomes the actual range measured modulo R_{ua}: $R_a = R$ modulo R_{ua}. It is then necessary to resolve the ambiguity (*disambiguate* the measurement), that is, determine R given R_a and R_{ua}. Unfortunately, the answer is not unique: there are an infinite number of ranges of the form $R_n = R_a + n \cdot R_{ua}$ that are consistent with the measurement R_a. However, as the range increases, the return power also decreases. If we consider targets of roughly comparable radar cross section (RCS)[1], and if we can define a maximum range R_{max} as that at which the return exceeds the minimum detectable signal, then range ambiguities are of no concern if $R_{max} < R_{ua}$ because the targets at ranges beyond R_{max} are below the receiver noise level and will not be detected. The range ambiguities, however, are a concern when targets at a

[1] RCS describes the amount of incident power scattered from a target back towards the radar when the target is illuminated by electromagnetic energy. More formal definitions of RCS are beyond the scope of this document. See [1] for more information.

range shorter than that of the given target have the same location on the time scale as those of the target of interest.

To illustrate the problem, consider the situation shown in Fig. 1.6. In this figure, the time between transmit pulses or PRI T is 200 μs. The unambiguous range is then 30 km. Now suppose there is a target at a range of 45 km from the radar. The time delay T_R for this range will be

$$T_R = \frac{2R}{c} = \frac{2\times 45\times 10^3}{3\times 10^8} = 300\ \mu\text{s}.$$

This means that the return from the first pulse would not be received until after the second pulse is transmitted, the return from second pulse would not be received until after the third pulse is transmitted, and so on. Since all of the transmit pulses are the same, there is no way of associating a received pulse with the corresponding transmit pulse, and in this case due to the fact the target range delay is greater than the transmit time between pulses, the received pulse k will be associated with the most recent transmit pulse k+1. The measured range delay would be 100 μs, which when used to compute range would give an apparent range of

$$R_a = \frac{c\times 100\times 10^{-6}}{2} = 15\ \text{km}.$$

Note that R_a is the actual range of the target less the unambiguous range of the radar.

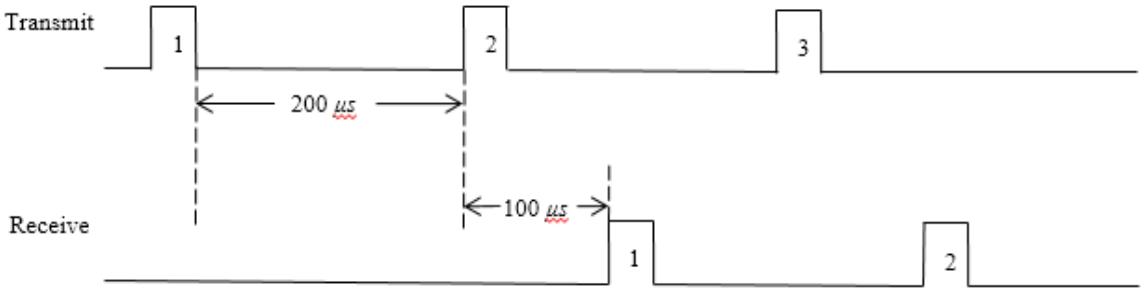

Fig. 1.6 Range ambiguity.

The identical problem exists with Doppler (velocity) measurements, since the actual Doppler shift will be aliased into the interval ($-PRF/2$, $+PRF/2$) so that Doppler shifts outside the range $\pm PRF/2$ will result in Doppler ambiguities. Analogous to the case of range measurements where the true range could be the apparent range plus or minus multiples of the unambiguous range, the true Doppler shift F_D could be its apparent value plus or minus multiples of the PRF. As shown in Fig. 1.4, the spacing between the consecutive spectral lines increases with PRF. The implication is that if the maximum Doppler frequency F_{Dmax} to be expected based on a priori information about expected targets in the radar scenario does not exceed the PRF, then there will be no Doppler ambiguities. The criterion for avoidance of Doppler ambiguities is then $PRF > F_{Dmax}$ which means that we must choose a high enough value for the PRF to avoid Doppler ambiguities. This is in direct conflict with the criterion for avoidance of range ambiguities, which are minimized by keeping the PRF low. Thus, there is a tradeoff between high PRF for Doppler ambiguity avoidance and low PRF for range ambiguity avoidance in pulse Doppler radars. For this reason, while the choice of high or low PRF depends on system requirements, pulse Doppler radar systems often use medium-PRF sets (3-30 kHz) which provide a good compromise between ambiguous range and Doppler measurements. Ambiguity resolution techniques are then used to find true ranges and velocities of the targets.

Need for Multiple PRFs

Targets separated by an integer multiple of the maximum unambiguous range cannot be distinguished in pulse Doppler radars using pulses repeated at the same interval, i.e. using a single PRF. For this reason, the range-Doppler ambiguity resolution problem in pulse Doppler radars is addressed by repeating the basic pulse Doppler measurement with several different pulse repetition frequencies, producing different aliasing characteristics. Each of the PRFs yields ambiguous measurements, but the combined measurements from a well-chosen set of the PRFs can eliminate all ambiguities out to

distances determined by the radar's sensitivity. One of several algorithms is then applied to determine the true range/velocity pairs that are consistent with all the measurements.

Another reason for using multiple PRFs is that some targets may fall into a range/velocity cell that is "blind" in some PRFs but visible in others. Blind zones in range are caused by the pulse eclipsing phenomenon in monostatic radars, when the echo signal is received during the time another pulse is being transmitted, and the receiver is not connected to the antenna. The eclipsed region in the range-Doppler detection space is τ seconds long, from nT to ($nT+\tau$), and repeats at ranges corresponding to the PRI T. A target would not be detected if its echo comes back in these time intervals. Blind zones in Doppler are caused by clutter interference. Doppler blind zones repeat at an interval equal to the radar PRF and span velocity cells masked by the strong main lobe clutter interference in the near-end of the spectrum every time a pulse is transmitted. Targets at these Dopplers would go undetected due to low signal-to-interference ratio. Depending on the pulse width and clutter spread, a considerable portion of the range/velocity space of interest may be blind.

The blind range and velocity cells can be depicted on a blind zone map as shown in Fig. 1.7. The black stripes in the map are the blind zone cells where the targets are presumed undetectable, while the white areas represent the range-Doppler cells where targets are assumed detectable. Different values of PRF result in similar looking, although subtly different, blind zone maps since regions of blindness differ depending on the precise value of PRF. By selecting several PRFs, the regions of blindness are dispersed so targets that may be blind in one PRF may become visible in others. The greater the number of PRFs used, the greater the probability that any given target would be detected in a significant number of PRFs.

A common way of taking multiple-PRF measurements in pulse Doppler radars is to transmit a schedule of N different PRF bursts during the time-on-target, and to use M out of the N measurements to decode range and Doppler information unambiguously.

Typically, the total number of PRFs *N* may be in the range of 5 to 9; a value of *N*=8 is often used [3]. To resolve the range and Doppler ambiguities, target detections are required in a minimum number of PRFs *M*. A 3 of 8 schedule is common [3]. The design must consider detection performance as well as other factors such as the effects of blind zones.

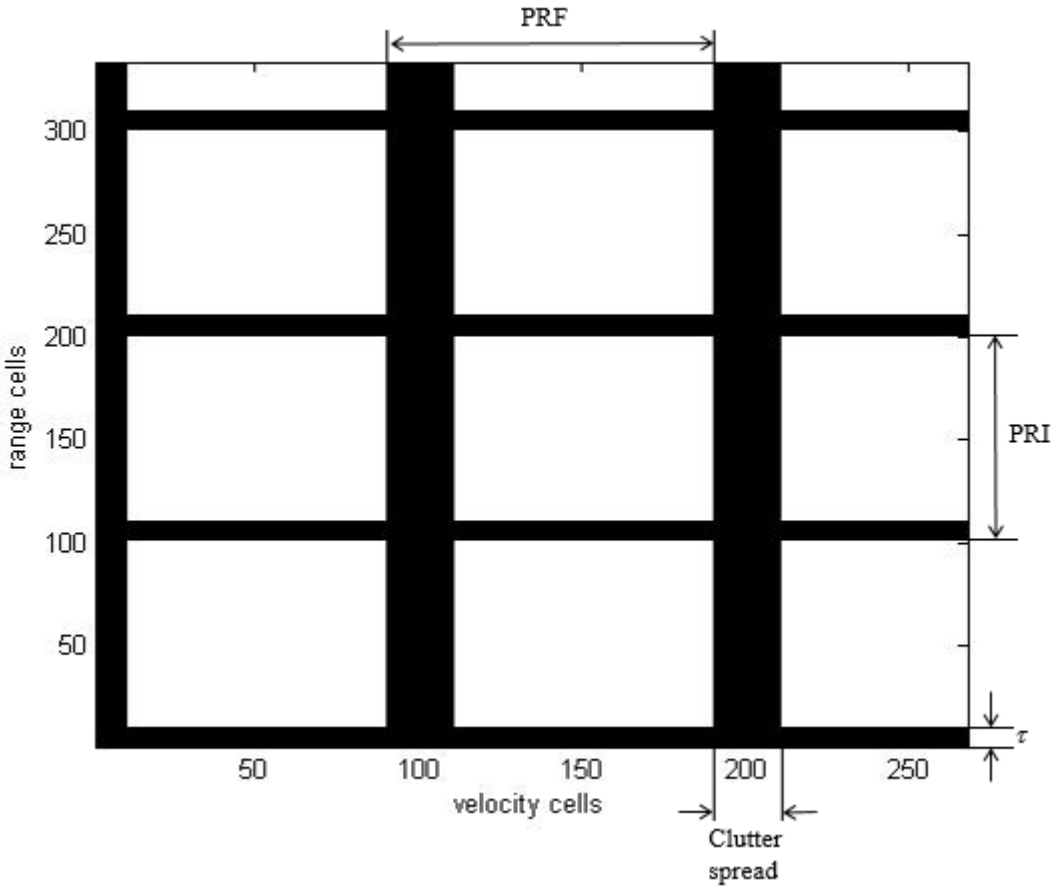

Fig. 1.7 Blind zone map of a 10 *KHz* PRF range-Doppler matrix.

Current Methods for Ambiguity Resolution

Common algorithms for ambiguity resolution include the Chinese Remainder Theorem (CRT) and the coincidence algorithm. The CRT is an analytic procedure for calculating the unambiguous range from the measured range using multiple *PRFs*. This theorem states that for positive integers *r* and *s* that are relatively prime and for any two arbitrary integers *a* and *b*, there will be a number *Q* such that [4]

$$a \bmod r = Q = b \bmod s. \tag{1.1}$$

To apply this to range ambiguity resolution, a and b translate to the actual ranges of the target measured with PRFs having an unambiguous range of r and s respectively. The system is then solved for Q which gives the actual range to the target. At least (k+1) PRFs are required to resolve k targets. All PRIs have to be subdivided into an integer number of range resolution cells and the number of range cells in the PRIs must be relatively prime. Let n_{i} be the number of range cells in the i^{th} PRF, and R_i be the respective apparent range cell measurement carried out using the i^{th} PRF. The unambiguous range R_{ua} is then given by the CRT as:

$$R_{\mathrm{ua}} = \left(\sum_{i=1}^{k} \alpha_i R_i \right) \mathrm{modulo} \left(\prod_{j=1}^{k} n_j \right). \tag{1.2}$$

where the α's are given by

$$\alpha_i = \beta_i \prod_{j=1,\, j \neq i}^{k} n_j \tag{1.3}$$

The β's are the smallest integers such that

$$\left(\prod_{\substack{i=1 \\ j=1,\, j \neq i}}^{k} \beta_i n_j \right) \mathrm{modulo}\, n_i = 1. \tag{1.4}$$

The application of the basic CRT approach for ambiguity resolution can be best explained with the help of an example. Consider a multiple-PRF radar system transmitting with a pulse length of 10 μs followed by a reception period of 110 μs (11 range bins) on the first PRF, 120 μs on the second PRF (12 range bins) and 130 μs on the third PRF (13 range bins). Now suppose that a target is detected in bin 8 on the first PRF, bin 7 on the

second PRF and bin 6 on the third PRF. Let the true range to the target be bin x, then we can define the problem as:

$$\begin{aligned} 8 &\equiv x \bmod 11 \\ 7 &\equiv x \bmod 12 \\ 6 &\equiv x \bmod 13 \end{aligned} \tag{1.5}$$

Solving the congruence equations in (1.5) using the CRT approach, we find $x = 19$ which corresponds to a time delay of 190 μs.

The basic CRT approach is inherently very sensitive to measurement errors which can result in range and velocity errors. A small range error on a single PRF can cause a large error in the disambiguated range. To illustrate the effect of errors in the measurement, we repeat the same example with an erroneous measurement in one of the PRFs. Suppose an error in the third PRF measurement caused the target to be detected in bin 7 instead of bin 6. The true range to the target then comes out to be bin 943, which is incorrect and is many times the actual range R_{ua}.

The CRT techniques are simple to implement in hardware but the algorithm works only for very few combinations of PRFs. PRF set must satisfy the ambiguity resolution constraints for range and Doppler given by Eq. (1.6) and Eq. (1.7) respectively. These constraints must be satisfied for all combinations of M PRFs out of the total N PRFs, since the target may be detected in any of these combinations.

$$LCM\left(PRI_1,\ PRI_2 \ldots\ PRI_M\right) \geq \frac{2R_{max}}{c}, \tag{1.6}$$

$$LCM\left(PRF_1,\ PRF_2 \ldots\ PRF_M\right) \geq f_{Dmax}. \tag{1.7}$$

The CRT also applies additional constraints on PRF selection for Doppler ambiguity resolution that make it virtually impossible to find PRF sets satisfying both the conditions

for range and Doppler ambiguity resolution. The CRT algorithm requires the number of range cells in all combinations of *M* out of *N* PRIs must be coprime. Furthermore, it may be desirable to use one set of PRFs to resolve range and a different set of PRFs to resolve velocity [3]. For more details, the reader is referred to [5].

The coincidence approach is a graphical application of the basic CRT principle and works by concatenating the measurements for each PRF and declaring a target at the bin location which is consistent with all the multiple-PRF measurements, i.e. where detection exists in all of the PRFs. For each PRF in which a target is detected, all possible ambiguous ranges and velocities are computed out to the maximum range and velocity of interest. Fig. 1.8 illustrates the graphical representation of the data presented in the above example. Next the replicated measurements are concatenated for each *PRF*, and the unambiguous range to the target is found from the range bin with coincident detections all three PRFs. As shown in Fig. 1.9, the detections are coincident in range bin 19 which is the same result as obtained from the classical CRT.

Fig. 1.8 Detection data from three PRFs.

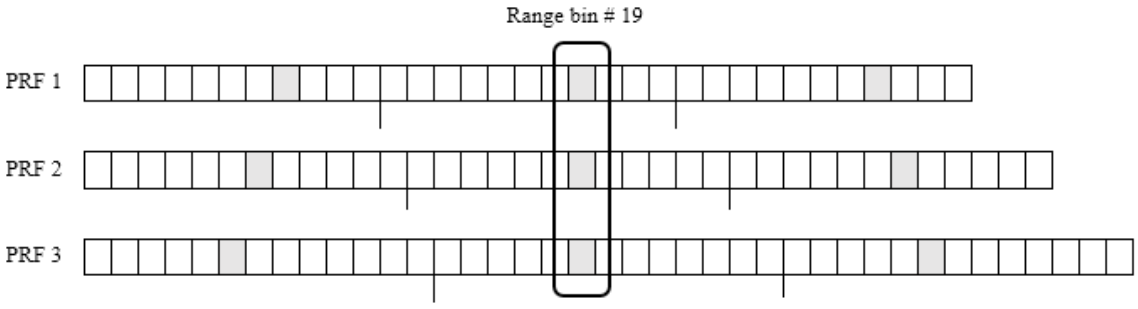

Fig. 1.9 Concatenated detection data and coincidence.

As noted before, lower values of PRF favor ambiguity resolution in range, whereas higher values of tend to favor Doppler ambiguity resolution. Full decodability in range and Doppler requires a significant spread of PRF values. As in the CRT algorithm, it may be desirable to use one set of PRFs to resolve range and a different set of PRFs to resolve velocity.

The coincidence algorithm and CRT are mainstream techniques used in practical systems. More sophisticated CRT-based algorithms and a number of alternative methods of ambiguity resolution have been developed and reported in the radar literature [6], [7].

Overview of the Thesis Report

This thesis report is organized into six chapters. Chapter 1 describes the range and Doppler measurement process, the ambiguity in the measurements and the conventional ambiguity resolution techniques. Chapter 2 gives an overview of the detection process in radars explaining the Neyman-Pearson criterion that leads to a binary detection map. Key characteristics of post-detection data are noted and the chapter concludes with an explanation of the mathematical model developed to solve the ambiguity resolution problem using L^1 minimization. Chapter 3 walks the reader through the basics of norm minimization and compressive sensing theory. The significance of L^0/L^1 equivalence and the use of the L^1 minimization technique for our sparse reconstruction problem is also discussed. Chapter 4 presents the simulation setup and results using two different L^1 minimization algorithms with varying radar parameters. The performance of the technique in the presence of errors introduced by real world effects like false alarms and missed detections is shown in Chapter 5. Finally, the report concludes in Chapter 6 with a discussion on results obtained in Chapter 4 and Chapter 5.

CHAPTER 2

DETECTION PROCESS AND POST-DETECTION DATA

Detection refers to the process of deciding whether some phenomenon is present or not in a given situation. In communication systems, decision theory is used to detect which one among a set of mutually exclusive alternatives is correct. For example, it is used to establish whether a "1" or a "0" was transmitted on a digital communication channel in the presence of noise. Radar detection involves the process of deciding whether a target is present or not on the basis of radar measurements in range, Doppler or angle. These measurements are corrupted by not only thermal noise but also unwanted echoes, which may originate from passive external sources not designated as "target" by the radar operator, or may be a result of active jamming from a source transmitting electromagnetic energy at the radar frequency. The term *clutter* is used in radars to refer to objects that generate unwanted returns which may interfere with the returns from the target. Often, the clutter signal level is much higher than the receiver noise level in at least some range-Doppler cells. Like thermal noise, clutter echoes are random but clutter power may vary from one bin to the next. The receiver noise, clutter returns and jamming, if any, are the main obstructions in detection of a target and are collectively referred to as *interference.* The received echo in radars, therefore, can be a result of interference only, or reflections from a target with some degree of interference.

Detection Process in Radars

The decision to choose between one of these two mutually exclusive events is carried out through the process of hypothesis testing, and the events are called hypotheses. These events, in addition to being mutually exclusive, are collectively exhaustive. This means that the sample outcome of the experiment must be one and only one of these events,

i.e. in each performance of the experiment, one and only one of the hypotheses is correct. In radars, hypothesis H_0 or the *null hypothesis* is used to denote the case of interference only, whereas H_1 is the event when the data sample represents target and interference.

A decision is made between the possible hypotheses for each sample value y of the observation vector which represents a range or range-Doppler cell, and the process is repeated for every cell. Because of the statistical nature of both interference in radar systems and returns from a target, these decisions are initially made using a probabilistic approach. As an example, suppose that based on the measured sample y, it is determined that hypothesis H_0 is correct with probability 2/3 and hypothesis H_1 is correct with probability 1/3. Simply making a decision to choose hypothesis H_0 and ignoring other probabilities seems to be throwing away much of the gathered information. But, just like in communication systems where the user wants to receive a specific message rather than a set of probabilities, in radar we want to know if the target is present or not, so a choice between H_0 and H_1 must be made.

To make this decision, the random vector of measurements under test **y** is first statistically described using a probability density function (PDF). The detection process then requires the calculation of the conditional probabilities

$p_y(y|H_0)$, i.e. the PDF of **y** if there was no target (interference only),

$p_y(y|H_1)$, i.e. the PDF of **y** if a target was present.

These conditional PDFs are also known as likelihood functions in hypothesis testing. Based on these likelihood functions, the goal of the detection process is to decide which of the two hypotheses, H_0 or H_1, best explains the radar measurements based on a set rule for making the optimum choice. This decision can be wrong sometimes which leads to the notion of defining the probability of detection P_D and the probability of false alarm P_{FA}. P_D is defined as the probability of rejecting the null hypothesis H_0 and choosing hypothesis H_1 when a target is present. P_{FA} is the probability of rejecting the null hypothesis H_0 and choosing hypothesis H_1 when the target is, in fact, not present. The four probabilities

associated with a binary decision, and the way they are mathematically related, are shown in Table 2.1. In radar, typical P_{FA}s vary widely but they are commonly in the range of 10^{-3} to 10^{-8}. P_D depends on many things but it is desirable to have a P_D greater than 0.8 and preferably greater than 0.9.

TABLE 2.1 Binary decision outcomes and probabilities.

Decision	**Event**	
	Target not present	*Target present*
H_0	Correct decision Probability = 1-α	Error of the second kind Probability = β
H_1	Error of the first kind Probability = P_{FA} = α	Correct decision Probability = P_D = 1-β

The observation space $\mathcal{Y}$ is partitioned into two regions $\mathcal{R}_0$ and $\mathcal{R}_1$. If $\mathbf{y} \in \mathcal{R}_0$, H_0 is chosen whereas if $\mathbf{y} \in \mathcal{R}_1$, H_1 is chosen. P_D and P_{FA} can then be defined using the conditional PDFs $p_{\mathbf{y}}(\mathbf{y}|H_0)$ and $p_{\mathbf{y}}(\mathbf{y}|H_1)$ as

$$P_D = \int_{R_1} p_y\ (y \mid H_1)\, dy, \tag{2.1}$$

$$P_{FA} = \int_{R_1} p_y\ (y \mid H_0)\, dy. \tag{2.2}$$

A number of possible criteria can be used to make decisions on choosing $\mathcal{R}_0$ and $\mathcal{R}_1$. Commonly used criteria include maximum likelihood, Neyman-Pearson, minimum error probability and Bayes minimum risk rule. All these criteria lead to a comparison between a function of the observation, namely the *likelihood ratio* $\Lambda(y)$, with a suitable threshold. The likelihood ratio is defined as

$$\Lambda(y) = \frac{p_y(y \mid H_1)}{p_y(y \mid H_0)}. \tag{2.3}$$

Neyman-Pearson Criterion for Hypothesis Testing

The most commonly used rule for making the optimum choice in radars is the Neyman-Pearson optimization criterion. In order to make a good decision, it is desirable that the false alarm probability P_{FA} be as low as possible, while the detection probability P_D should be as high as possible. However, Eq. (2.1) and Eq. (2.2) show that P_D and P_{FA} are integrals over the same limits, so that P_{FA} grows with P_D for a given system design. The Neyman-Pearson rule is based on the strategy of fixing one of the two probabilities at a given value while the other is optimized. Typically, a system-specific value α_0 is established for P_{FA} and P_D is maximized subject to the constraint $P_{FA} \leq \alpha_0$ [1].

As an example, suppose the statistics of a data sample y are related to the events H_0 and H_1 by the following Gaussian PDFs with mean μ and variance β.

$$p_y\ (y \mid H_0) = \frac{1}{\sqrt{2\pi}} e^{-y^2/2\beta}$$

$$p_y\ (y \mid H_1) = \frac{1}{\sqrt{2\pi}} e^{-(y-\mu)^2/2\beta}$$

The above equations show that the detection decision here is to determine if the constant μ is present or not. The signal-to-noise ratio for this problem is μ^2/β and the likelihood ratio is

$$\Lambda(y) = \frac{e^{-(y-\mu)^2/2\beta}}{e^{-y^2/2\beta}} = e^{\left(\frac{\mu y}{\beta} - \frac{\mu^2}{2\beta}\right)}$$

Proceeding with the LRT

$$e^{\left(\frac{\mu y}{\beta} - \frac{\mu^2}{2\beta}\right)} \begin{matrix} H_1 \\ > \\ < \\ H_0 \end{matrix} \eta$$

Taking the natural logarithm on both sides and simplifying,

$$\left(\frac{\mu \mathrm{y}}{\beta}-\frac{\mu^2}{2\beta}\right) \underset{H_0}{\overset{H_1}{\gtrless}} \ln\eta$$

Rearranging to have only the data samples *y* on the left hand side and moving all constants to the right hand side, we get

$$y \underset{H_0}{\overset{H_1}{\gtrless}} \frac{\beta \cdot \ln\eta}{\mu}+\frac{\mu}{2\beta} \equiv T \tag{2.4}$$

The threshold *T* can be computed from the right hand side of Eq. (2.4) by expressing P_{FA} in terms of *y*, setting it equal to α_0 and then solving for *T*. Using Eq. (2.2), we can write

$$P_{FA}=\int_T^{\infty} \frac{1}{\sqrt{2\pi}} e^{-y^2/2\beta}\, dy = \alpha_0 \tag{2.5}$$

The integral in Eq. (2.5) is the tail probability of a standard normal distribution, commonly known as the *Q-function* and expressed as $Q(T)$. It is then straightforward to find the threshold *T* given $Q(T) = \alpha_0$. Once the threshold is set, P_D can be determined using Eq. (2.1)

$$P_D=\int_T^{\infty} \frac{1}{\sqrt{2\pi}} e^{-(y-\mu)^2/2\beta} dy \tag{2.6}$$

The above analysis shows that the Neyman-Pearson criterion is the first step in obtaining the achievable combinations of P_D and P_{FA}. The two Gaussian PDFs presented in the above example are shown in Fig. 2.1 with the value of constants arbitrarily chosen as μ=5 and β=9. A threshold value of 6 was also arbitrarily selected to highlight the areas representing P_D and P_{FA}.

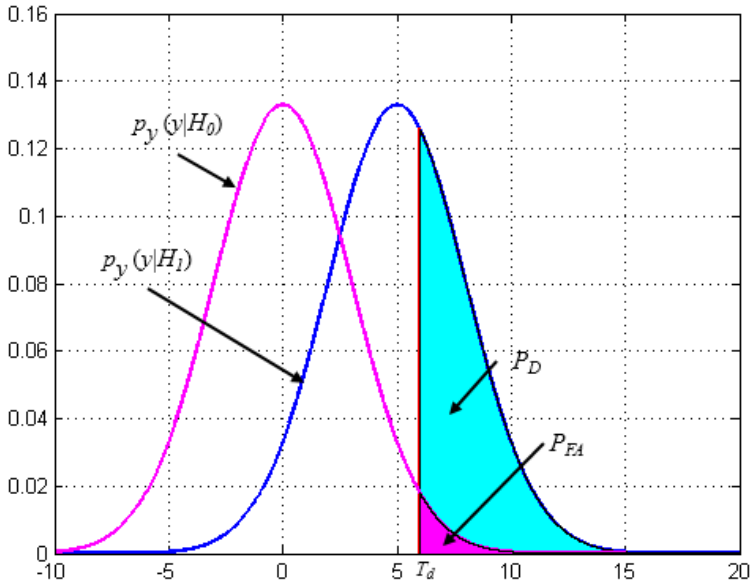

Fig. 2.1 P_D and P_{FA} as thresholded areas of conditional PDFs.

Fig. 2.1 suggests that P_D can be increased for a given P_{FA} by reducing the overlap of the two PDFs. This translates to having either a greater value of the constant μ or a smaller value of the noise variance β, both of which are tantamount to improving the signal-to-noise ratio. This implies that the tradeoff between P_D and P_{FA} can be improved by increasing the SNR.

Once a matrix of data is collected and a range-Doppler matrix formed, the threshold test procedure described above is repeated for each range-Doppler bin. The result is a binary detection map: target present or target not present in each bin.

Post-detection Data Modeling

The purpose of the discussion so far is to introduce the reader to the radar detection process and to develop a familiarity with the outcome of the threshold detection. We will build on this knowledge to state the key characteristics of the post-detection data which prompted the use of L^1 minimization methods for ambiguity resolution in radars. We also use this knowledge to construct a linear mathematical model for the problem consisting of a system of underdetermined equations.

In this project, we consider post-detection ambiguity resolution. "Post-detection" means that the data is examined after threshold detection has been performed. In each range or range-Doppler bin, either a target was detected at that location, or it wasn't. The threshold detection results can, therefore, be represented as either a "1" or a "0" for each range-Doppler bin tested, where "1" represents the presence of a target and "0" represents the interference only case.

It is important to note that the post-detection data, in addition to being binary, is also *sparse*, meaning that the radar target detections are limited to only a few of the total number of range-Doppler bins. In real environments most range or Doppler bins will *not* contain a detectable target; detections will be present in only a small fraction of the bins. It is assumed here that this is always the case and we will exploit the sparseness of the post-detection data to solve the ambiguity resolution problem.

Mathematical Model for Post-detection Data

Chapter 1 considered the process of multi-PRF measurements and the resulting range and Doppler ambiguities. We can now proceed to state the ambiguity resolution problem mathematically. First, consider a range-only problem. Consider a system transmitting pulses with a PRI corresponding to $R_{ua} = 4$ range bins. Assume the sensitivity of the radar is such that targets could possibly be detected at ranges out to the 7^{th} range bin.[2] Now suppose that in fact there are detectable targets at ranges corresponding to the 2^{nd} and 7^{th} range bins. For the second and subsequent pulses, these will result in detections that appear to occur in range bins 3 (bin 7 modulo 4) and 2 (bin 2 modulo 4). This measurement process can be represented as the following $m \times n$ set of linear equations,

[2] These ranges are unrealistically short, but are convenient for writing out explicit equations. Real radars might have PRIs corresponding to hundreds to a few thousand range bins, and be sensitive enough to detect targets at those ranges or further.

where the number of unknowns n is the number of range bins over which targets might be detected, and the number of measurements m is the number of range bins in the unambiguous range interval:

$$\begin{bmatrix} 0 \\ 1 \\ 1 \\ 0 \end{bmatrix} = \begin{bmatrix} 1 & 0 & 0 & 0 & 1 & 0 & 0 \\ 0 & 1 & 0 & 0 & 0 & 1 & 0 \\ 0 & 0 & 1 & 0 & 0 & 0 & 1 \\ 0 & 0 & 0 & 1 & 0 & 0 & 0 \end{bmatrix} \begin{bmatrix} 0 \\ 1 \\ 0 \\ 0 \\ 0 \\ 0 \\ 1 \end{bmatrix} \tag{2.7}$$

For a single PRF and a maximum detection range $R_{max}>R_{ua}$, $n > m$ so that the solution is underdetermined. Notice that the matrix describing this system is a 4×7 binary Toeplitz matrix. Denoting this matrix as $T_{m,n}$, Eq. (2.7) becomes simply

$$\mathbf{y} = T_{4,7}\mathbf{x}. \tag{2.8}$$

If the measurements were repeated with a different PRF, e.g. one with 5 bins in the unambiguous range interval, a new system of equations described by a 5×7 binary Toeplitz matrix would be generated.

Problem Formulation

The measurements made with a single PRF can be expressed in the form of a Toeplitz matrix applied to the actual target distribution in range or Doppler as shown in Eq. (2.7). In the case of multi-PRF measurements, the individual Toeplitz matrices for all PRFs can be vertically concatenated to form a combined measurement matrix. The linear system of equations thus formed represents all of the measured data. Depending on the number of PRFs, the number of unaliased range bins n, and the sum of the number of range bins in the unambiguous range for each of the PRFs representing the total number of measurements m_s, the resulting system of equations may be either over or underdetermined.

Continuing with the same example, consider a three-PRF case with the truth vector $\mathbf{x} \in \mathcal{B}^7$ where $\mathcal{B}$ denotes a binary space, and the three PRFs corresponding to unambiguous ranges of 4, 5 and 6 range bins. We therefore have the following three sets of equations:

$$\begin{aligned} \mathbf{y}_1 &= T_{4,7}\mathbf{x} \\ \mathbf{y}_2 &= T_{5,7}\mathbf{x} \\ \mathbf{y}_3 &= T_{6,7}\mathbf{x}. \end{aligned} \tag{2.9}$$

We form a single system of linear equations $\mathbf{y} = A\mathbf{x}$ with measurement matrix A ($m_s \times n$) by concatenating the three Toeplitz matrices together as shown in Eq. (2.13). A is then a binary $\mathcal{B}^{15\times 7}$ matrix with 15 linear measurements of the unknown vector $\mathbf{x}$.

$$\mathbf{y} = A\mathbf{x} = \begin{bmatrix} T_{4,7} \\ T_{5,7} \\ T_{6,7} \end{bmatrix} \mathbf{x} \tag{2.10}$$

where

$$A = \begin{bmatrix} 1 & 0 & 0 & 0 & 1 & 0 & 0 \\ 0 & 1 & 0 & 0 & 0 & 1 & 0 \\ 0 & 0 & 1 & 0 & 0 & 0 & 1 \\ 0 & 0 & 0 & 1 & 0 & 0 & 0 \\ 1 & 0 & 0 & 0 & 0 & 1 & 0 \\ 0 & 1 & 0 & 0 & 0 & 0 & 1 \\ 0 & 0 & 1 & 0 & 0 & 0 & 0 \\ 0 & 0 & 0 & 1 & 0 & 0 & 0 \\ 0 & 0 & 0 & 0 & 1 & 0 & 0 \\ 1 & 0 & 0 & 0 & 0 & 0 & 1 \\ 0 & 1 & 0 & 0 & 0 & 0 & 0 \\ 0 & 0 & 1 & 0 & 0 & 0 & 0 \\ 0 & 0 & 0 & 1 & 0 & 0 & 0 \\ 0 & 0 & 0 & 0 & 1 & 0 & 0 \\ 0 & 0 & 0 & 0 & 0 & 1 & 0 \end{bmatrix}$$

The solution to the overdetermined system of equations so formulated is the truth vector **x** with unambiguous range information. It is, however, the underdetermined case with the number of measurements much less than the number of unknowns ($m_s << n$) that is of more practical interest and hence will be discussed in the subsequent chapters in detail.

Doppler Extension

The ambiguity resolution problem can be easily extended in another dimension to account for a pulse Doppler measurement process with both range and Doppler ambiguities by vectorizing the two-dimensional range-Doppler grid. Once the dimensions of the range-Doppler grid have been defined – the range bins based on the maximum range and range bin spacing, and the Doppler cells based on the PRFs, the estimated range of Doppler shifts and Doppler bin spacing – we form the range and Doppler binary Toeplitz matrices T_R and T_D respectively in the same way as shown in Eq. (2.7). T_R and T_D are then combined for each PRF into one binary matrix A_{PRF} by taking their Kronecker product. The order of the Kronecker product is dictated by the order in which the range-Doppler grid of Fig. 1.2 is vectorized: if the columns of the range-Doppler matrix are stacked into a single column vector **x**, then

$$A_{PRF} = T_D \otimes T_R, \tag{2.11}$$

where $\otimes$ represents the Kronecker product. As in the one dimensional case, a single system of linear equations is then formed by vertically concatenating the individual A_{PRF} matrices for multiple PRFs to form the measurement matrix $A(m_s \times n)$ of the combined system that represents all of the measured data, similar to Eq. (2.10). The total number of measurements m_s in the concatenated data is now given by adding up the products of the number of range cells in the unambiguous range and the number of velocity cells in the unambiguous velocity measurements of each PRF, and the total number of unknowns n is

now the product of the number of range bins and the number of Doppler cells over which the target might be detected.

Assumptions

It is assumed throughout this report that the post-detection data is sparse. The sparsity k is defined as the number of targets present in the post-detection data. In all simulations, k is taken to be a small fraction of the total number of range bins or range-Doppler bins. To obtain a realistic number of targets in the detection space in our simulations, we will assume a sparsity of the order of 1% of the total number of bins n for one dimensional range-only examples, and 0.01% of n for the two-dimensional range-Doppler simulations. For example, a range ambiguity resolution problem with $R_{\max} = 600$ range bins will have n=600, and a 1% target sparsity of 6 in the truth vector $\mathbf{x}$ would be a reasonable assumption. On the other hand, a range-Doppler simulation with $R_{\max}$=2000 range bins and the maximum detectable velocity $V_{\max}$=100 velocity cells will have n=200,000, and it is more realistic to assume a target sparsity of 0.01% in this case which gives 20 targets in the detection space.

The mathematical model described earlier results in a non-binary observation vector $\mathbf{y}$ in the case when two targets alias to the same location in $\mathbf{y}$, a phenomenon we refer to as a *collision*. Specifically, if two targets alias to the same bin in the observation vector, that measurement will have a value of two instead of one, so the measurement vector is no longer binary. For example, Eq. (2.7) had detectable targets in range bins 2 and 7 which appeared in range bins 2 and 3 in the aliased measurement made with a PRI of 4 range bins. If the targets were located in range bins 2 and 6, both the targets would fold over into range bin 2 in the aliased measurement. This is shown in Eq. (2.12).

$$\begin{bmatrix} 0 \\ 2 \\ 0 \\ 0 \end{bmatrix} = \begin{bmatrix} 1 & 0 & 0 & 0 & 1 & 0 & 0 \\ 0 & 1 & 0 & 0 & 0 & 1 & 0 \\ 0 & 0 & 1 & 0 & 0 & 0 & 1 \\ 0 & 0 & 0 & 1 & 0 & 0 & 0 \end{bmatrix} \begin{bmatrix} 0 \\ 1 \\ 0 \\ 0 \\ 0 \\ 1 \\ 0 \end{bmatrix} \tag{2.12}$$

The observation vector on the left hand side of Eq. (2.12) is not a possible outcome in the normal radar threshold detection process, which cannot distinguish when a threshold crossing is due to one or multiple coincident targets and therefore produces only a 0 or a 1 in the measurement vector. To model this behavior, if two distinct targets alias to the same apparent range bin, the integer values greater than 1 are clipped to a value of 1 representing the practical case of single target detection for a single threshold crossing. The clipping, however, results in a case of measurement error which must be dealt with for the correct unambiguous detection of all targets. Eq. (2.10) can be revised to include the clipping operation as:

$$\mathbf{y}_b = \mathrm{C}\{A\mathbf{x}\}$$

where C represents the clipping operation and $\mathbf{y}_b$ represents the observation vector restricted to binary values only. In Chapter 5, we will show that the clipping operation is equivalent to adding an error vector on the right hand side of Eq. (2.10) with a -1 at the corresponding location.

Additional sources of measurement errors such as false alarms and missed detections also deviate from the linear model presented in Eq. (2.7). The changes in the mathematical model to account for these errors and their effects on the ambiguity resolution process are discussed in Chapter 5.

CHAPTER 3

L^1 MINIMIZATION APPROACH TO AMBIGUITY RESOLUTION

In Chapter 2, we formulated a linear system of equations to model the ambiguous radar measurements in range and Doppler in the absence of errors, such that the solution to the system would be the unaliased truth vector. In this chapter we will review the different methods to solve such a system of equations with an emphasis on the cases when a unique solution does not exist.

Vector Norms

In analyzing methods for solving linear systems, we need to be able to measure the "size" of vectors in $\mathcal{R}^n$. The norm of a mathematical object is a quantity that in some sense describes the length or size of the object, and is commonly used without any additional annotation to refer to vector norms. A vector norm provides vector spaces and their linear operators with measures of size, length and distance. Defined on some vector space $\mathcal{V}$, the vector norm of a vector $\mathbf{x} = [x_1\ x_2\ \ldots\ x_n]$ is a real-valued function $\|\mathbf{x}\|$ that satisfies these three requirements:

a) Positivity: $\|\mathbf{x}\| > 0\ \forall\ \mathbf{x}$ except $\mathbf{x}=0$ and $\|\mathbf{x}\| = 0$ iff $\mathbf{x}=0$
b) Homogeneity: $\|\lambda\mathbf{x}\| = \lambda\|\mathbf{x}\| \forall\ \lambda \in \mathcal{R}$
c) Sub-additivity: $\|\mathbf{x}+\mathbf{y}\| \le \|\mathbf{x}\| + \|\mathbf{y}\| \forall\ \mathbf{x}, \mathbf{y} \in \mathcal{V}$

The most commonly encountered vector norm is the L^2 norm, also known as the Euclidean norm, given by:

$$\|\mathbf{x}\|_2 = \sqrt{x_1^{\,2} + x_2^{\,2} + \ldots + x_n^{\,2}}$$

There are many other types of norms. In fact, there exists a norm corresponding to every real number. Mathematically, for $n \in \mathcal{R}$, the L^n norm of a vector $\mathbf{x}$ is defined as

$$\|\mathbf{x}\|_n = \left[\sum_i |x_i|^n \right]^{1/n} \tag{3.1}$$

The special cases n=0 and n=∞ are not proper "norms" by definition of Eq. (3.1). The L^0 norm of a vector **x** is defined as the total number (#) of non-zero elements in **x,** and the L^∞ norm is defined as the maximum of the absolute values of its components. Table 3.1 gives the values of different vector norms for a vector **x** = [1, -2, 0, 0, 3].

$$\|\mathbf{x}\|_0 = \#(i \,|\, x_i \neq 0)$$

$$\|\mathbf{x}\|_\infty = \max_i |x_i|$$

TABLE 3.1 Values of different vector norms for **x** = [1, -2, 0, 0, 3].

Type of norm	**Numerical value**
$\|\mathbf{x}\|_0$	3.000
$\|\mathbf{x}\|_1$	6.000
$\|\mathbf{x}\|_2$	$\sqrt{14} \approx 3.742$
$\|\mathbf{x}\|_3$	$36^{1/3} \approx 3.302$
$\|\mathbf{x}\|_\infty$	3.000

A unit ball is defined as the set of all vectors of norm 1, and hence the concept of unit ball is different in different norms: in a two-dimensional vector space, the unit ball for the L^1 norm is a square with vertices at (1,0), (0,1), (-1,0) and (0,-1) while for the L^2 norm, it is the well-known unit circle. This is shown in Fig. 3.1. The basic properties of a norm always make the unit ball a closed convex set symmetric about the origin. A convex set is a set of elements from a vector space such that all the points on the straight line between any two points of the set are also contained in the set, i.e. a set S is convex if for each $x_1, x_2 \in S$, the line segment $\lambda x_1 + (1-\lambda)x_2 \in S$ for $\lambda \in (0,1)$. It is important to note that the unit ball of the L^1 norm in $\mathcal{R}^n$ is an n-dimensional octahedron which is "pointy" while the unit ball of the L^2 norm in $\mathcal{R}^n$ is a generalized sphere which is round and "smooth". This is an

important detail in the context of minimization problems and one of the major reasons why an L^1 minimized solution is different from a minimum L^2 solution.

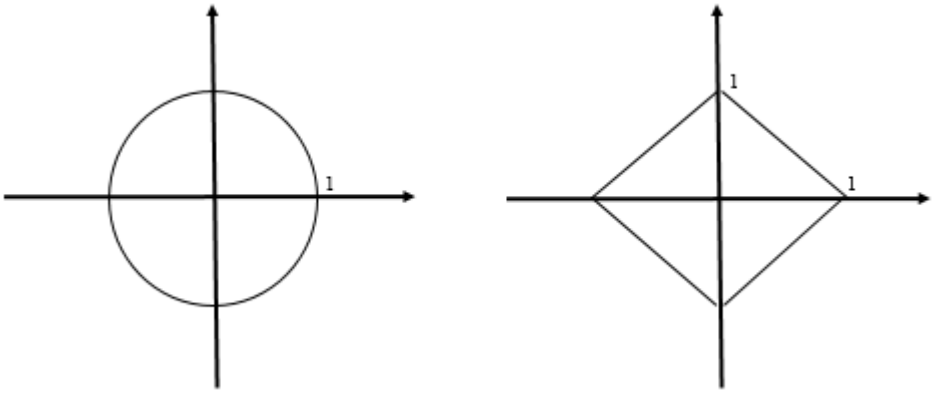

Fig. 3.1 Unit ball for L^2 norm (left) and L^1 norm (right) in $\mathcal{R}^2$.

Linear Systems of Equations with Non-Unique Solutions

A system of linear equations either has no solutions, a unique solution or infinitely many solutions. It is said to be consistent if it has at least one solution and inconsistent if there are no solutions. Many problems in applied science do not have a unique solution and require solving linear equations of the form $\mathbf{y}=A\mathbf{x}$ approximately. Approximate solutions to linear systems lead to the notion of *residuals*, defined as the quantity $(\mathbf{y}-A\mathbf{x})$.

Over Determined Systems

As shown in chapter 2, A is a matrix with m rows and n columns. When $m>n$, i.e. the number of linearly independent observations is more than the number of unknowns, the system is said to be *overdetermined*. The picture is:

$$\begin{bmatrix} y_1 \\ \vdots \\ \vdots \\ y_m \end{bmatrix} = \begin{bmatrix} a_{11} & \cdots & a_{1n} \\ \vdots & & \vdots \\ & \ddots & \\ \vdots & & \vdots \\ a_{m1} & \cdots & a_{mn} \end{bmatrix} \begin{bmatrix} x_1 \\ \vdots \\ x_n \end{bmatrix}$$

There is, in general, no exact solution to an overdetermined system. Instead, we look for the solution **x** with the smallest residual error vector **y**-*A***x**, using some vector norm to determine the size of the error vector. In the least squares method, we look for the error vector with the smallest L^2 norm. Mathematically, we find a vector **x*** such that

$$\left\|\mathbf{y} - A\mathbf{x}^*\right\|_2 \leq \left\|\mathbf{y} - A\mathbf{x}\right\|_2, \ \forall \mathbf{x} \in \mathcal{R}^n$$

The least squares solution is very sensitive to outliers in **y** as they result in large residuals. The L^1 norm minimization, on the other hand, minimizes the sum of absolute values of the residual error as opposed to minimizing the sum of squares, i.e.

$$\left\|\mathbf{y} - A\mathbf{x}^*\right\|_1 \leq \left\|\mathbf{y} - A\mathbf{x}\right\|_1, \ \forall \mathbf{x} \in \mathcal{R}^n$$

L^1 minimization effectively puts much larger weight on small residuals (so large that it forces most of them to be zero) and less weight on large residuals because they are no longer squared. Thus, minimizing L^2 or L^1 norms can lead to very different solutions qualitatively, and the choice of one over the other depends on the nature of problem.

As a very elementary but illustrative example, consider the overdetermined system

$$\begin{bmatrix} 6 \\ 6 \end{bmatrix} = \begin{bmatrix} 2 \\ 3 \end{bmatrix} x$$

The solution of the first equation is x=3, while the solution of the second equation is x=2. To find the best solution given both constraints, we will need to choose as a compromise some number between 2 and 3. There is a simple method for solving overdetermined systems using least squares. The least squares solution **x*** is given by the formula

$$\mathbf{x}^* = (A^t A)^{-1}(A^t \mathbf{y})$$

when A^tA is non-singular (A^t denotes the transpose of A). The least squares solution for this example is approximately 2.31 and the residuals are 1.3846 and -0.9231. In contrast, if we minimize the L^1 norm of the error, we obtain x=2 and more importantly the residuals 2 and 0. Thus minimizing the L^1 norm produces a more sparse set of residuals.

Underdetermined Systems

In many systems of practical importance, the number of observations is often less than the number of unknowns. An *underdetermined* system is a system of linear equations in which there are more unknowns than constraints. In this case, A has fewer rows than columns ($m<n$) and the problem has, in general, infinitely many solutions, or no solutions when it is inconsistent. Depending on the desirable solution properties, we can pick the solution with minimum L^2 norm that has the minimum energy, or the one that minimizes the L^1 norm among all the solutions satisfying $\mathbf{y}=A\mathbf{x}$ as shown in Eq. (3.2) and (3.3) respectively.

$$\min_{\mathbf{x}\in\mathcal{R}^n} \|\mathbf{x}\|_2 \text{ subject to } \mathbf{y} = A\mathbf{x} \tag{3.2}$$

$$\min_{x\in\mathcal{R}^n} \|\mathbf{x}\|_1 \text{ subject to } \mathbf{y} = A\mathbf{x} \tag{3.3}$$

The fundamental difference between these solutions is again the sparsity of the minimum L^1 solution. Often, signals of interest can be conveniently represented in a domain such that that the unknown vector is sparse in the sense that most of its coefficients

are zero. This is known as the sparse representation. It is now well known that many real world signals such as audio, video, still images and biological measurements are either sparse or have a sparse expansion in another domain [8]. L^1 minimization methods have recently been shown to be very effective in developing sparse solutions to various sensing problems in these areas. If the right hand side of the system of equations happens to be sparse, then L^1 minimization often returns the "correct" answer.

As an example, consider an underdetermined system where m=256 and n=512 so that half of the measurements needed for a unique solution are missing. Create a sparse vector **x** and select the position of the non-zero coefficients at random. We proceed to solve the system by choosing the minimum L^1 norm solution subject to the constraint $A\mathbf{x}=\mathbf{y}$. Fig. 3.2 shows the L^1 minimized sparse reconstruction laid on top of the original distribution of non-zero coefficients in the vector **x**. It can be seen that the reconstruction is exact. This remarkable result shows that one can recover sparse solutions from underdetermined equations exactly in the absence of noise provided that the number of measurements is sufficient to solve the problem (this is explained in more detail later in this chapter). In contrast, the minimum L^2 norm solution shown in Fig. 3.3 bears little resemblance to the original data.

Figure 3.4 shows a histogram comparison of the minimum L^1 and minimum L^2 norm solutions. One particular characteristic of the L^1 norm solution is the enormous peak at zero which underlines the fact that a lot of the elements in the solution vector are actually exactly zero. The histogram of the components of minimum L^2 norm solution shows that most of the components lie in the range from -1 to +1 without a distinct peak at zero.

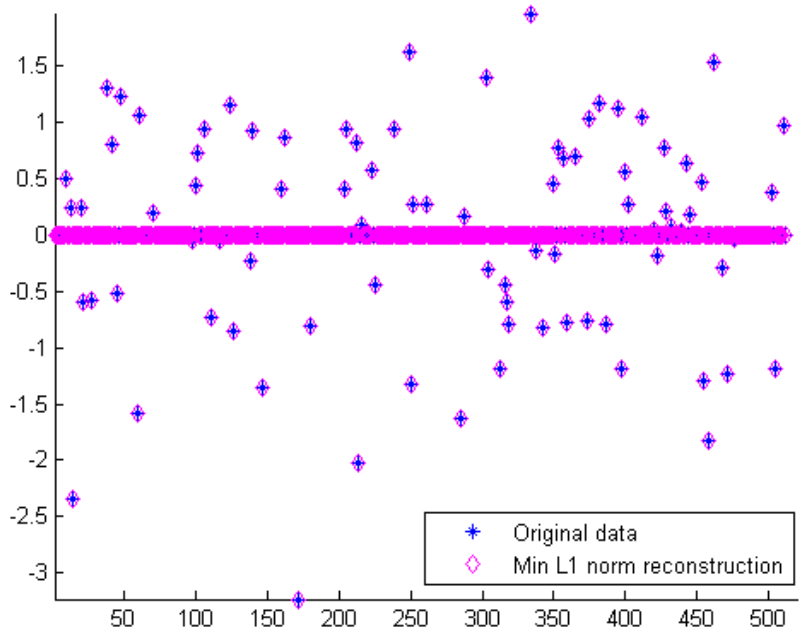

Fig. 3.2 Minimum L^1 reconstruction.

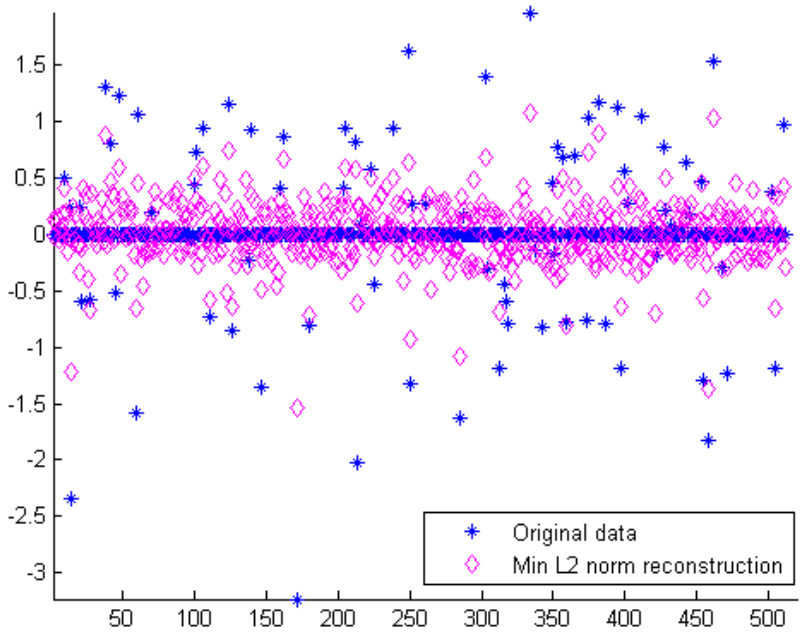

Fig. 3.3 Minimum L^2 reconstruction.

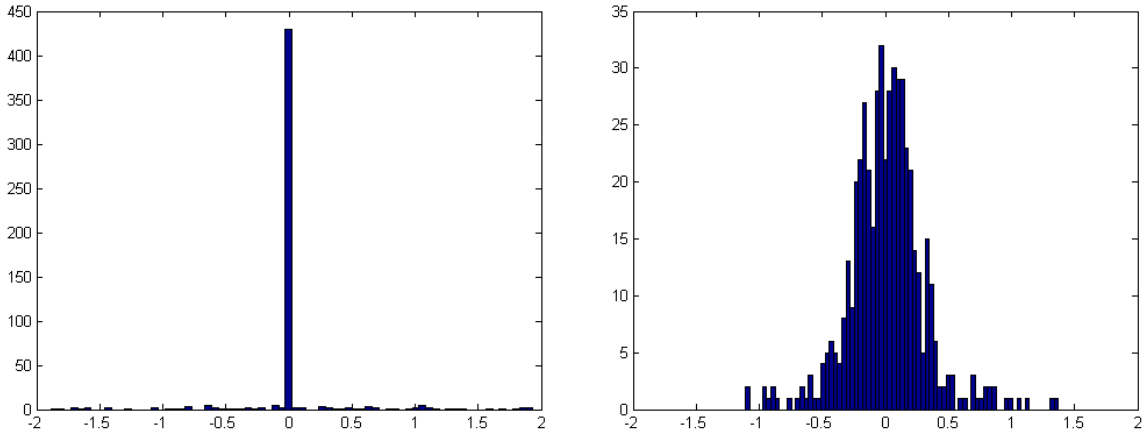

Fig. 3.4 Histogram comparison of minimum L^1 (left) and minimum L^2 (right) solutions.

Sparse Representation

Although the sparse representation problem has been studied for nearly a century in various forms, recent theoretical developments have generated a great deal of new interest in sparse signal representation. The problem definition assumes a given dictionary of "elementary" signals and models an input signal as a linear combination of dictionary elements with the provision that the representation is sparse, i.e., involves only a few of the dictionary elements. For example a signal $f(t)$ represented in a sparse basis ψ can be written as:

$$f(t) = \sum_i \alpha_i \psi_i(t)$$

The sparse representation of $f(t)$ implies that most of the coefficients $\{\alpha_i\}$ are zero. Finding sparse representations ultimately requires solving for the sparsest solution of an underdetermined system of linear equations. Such models arise often in signal processing, image processing, and digital communications. It is now well understood that many recorded signals such as music, photos, medical images and seismic data can be stored in compressed form by expressing them in terms of a linear basis, wherein many of the coefficients in the representation are zero or small enough to be ignored. This is the

rationale behind wavelet compression, JPEG image compression and MP3 audio compression, etc.

A large volume of work has established that the minimum L^1 norm solution to an underdetermined linear system is often, remarkably, also the sparsest solution to that system [9]. As noted earlier, pulse Doppler post-detection data is sparse. Our goal is to investigate whether L^1 techniques can provide an improved means of range/velocity ambiguity resolution in pulse Doppler radars. With the prior knowledge that the measured data is sparse, what we actually seek is the minimum L^0 "norm" solution[3], i.e. a solution with minimum number of non-zero components. However, finding the minimum L^0 norm solution is a well-known Np-hard problem because of its combinatorial nature. The L^1 norm solution, on the other hand, is a convex optimization problem and can be solved using techniques available in the literature. Fortunately, it has been shown that the minimum L^0 norm solution for any given unknown vector $\mathbf{x} \in \mathcal{R}^n$ is also given by the minimum L^1 norm solution, provided $\mathbf{x}$ is sufficiently sparse. Several studies have been conducted to establish the sparsity bound for L^0/L^1 equivalence in recent years [9]-[11], i.e. the maximum sparsity for which this property holds. Donoho [9] defines the *Equivalence Breakdown Point* of a matrix Θ, $EBP(\Theta)$, as the "maximal number N_z such that, for every α_0 with fewer than N_z non-zeros, the corresponding vector $S = \Theta\alpha_0$ generates a linear system $S = \Theta\alpha$ for which the L^0 and L^1 norm problems have identical unique solutions, both equal to α_0". Thus N_z is the maximum number of non-zeros for the equivalence to hold for a given linear system. $EBP(\Theta)$ depends only on Θ and for large n and m, it generally holds that

$$EBP(\Theta_{n,m}) = \sqrt{\frac{n}{2\log_2(mn)}}(1+\mathrm{O}(1))$$

---

[3] The quotation marks here acknowledge the fact that this is not a proper norm by definition.

where O(1) represents the process that takes a constant amount of time no matter how many elements there are. Thus for many matrices Θ, if there are no more than roughly $O(\sqrt{n})$ zeros, solutions to minimum L^0 and minimum L^1 norm are equivalent [12]. Furthermore, empirical examples were shown by Candès, Romberg and Tao [13], where equivalence held with as many as $n/4$ non-zeros for random partial Fourier measurement matrices.

Introduction to Compressed Sensing

Compressive sampling is a recent development in digital signal processing that offers the potential of high resolution capture of physical signals from relatively few measurements, typically well below the number expected from the requirements of the Shannon/Nyquist sampling theorem. The notion of compressed sensing proposes that a signal or image, unknown but supposed to be compressible by a known transform, can be subjected to fewer measurements than the nominal number of data points and yet be reconstructed accurately by solving an L^1 minimization problem. This technique combines two key ideas: sparse representation through an informed choice of linear basis for the class of signals under study; and incoherent measurements of the signal to extract the maximum amount of information from the signal using a minimum amount of measurements. Mathematical techniques required to implement compressive sampling include the development of novel types of linear bases (e.g. wavelet, curvelet, etc.), L^1 optimization to recover sparse representations, and design of optimal dual measurements exploiting the signal sparsity and incoherence between the domain in which the signal is assumed to be sparse and the domain in which the signal is sampled.

If the signal we wish to acquire is sparse in a basis ψ and the basis in which the signal is sensed is Φ, and both the sparsity waveforms ψ_i and sensing waveforms Φ_i are normalized, the *coherence* between these two systems $\mu(\psi,\Phi)$ is defined as the maximum correlation between the two bases times the signal dimension n.

$$\mu(\psi,\Phi) = \sqrt{n} \cdot \max_{i,k} \left| \psi_i \Phi_k \right|^2 \qquad (3.4)$$

where $< \psi_i, \Phi_k >$ represents the inner product between the elements of the two bases ψ and Φ. It follows that $\mu(\psi,\Phi) \in [1, \sqrt{n}]$. Equation (3.4) shows that coherence is a measure of similarity between the basis ψ and the basis Φ. It is maximum when the two bases are identical and minimum when, for example, ψ is the "spike basis" $\psi_i(t) = \delta(t-i)$ and $\Phi_k(t) = (1/\sqrt{n}) \cdot e^{j2\pi kt/n}$ is the Fourier basis. This corresponds to the typical sampling process in time and shows that the time-frequency pair have a mutual coherence of 1, and are therefore, maximally incoherent [14]. One way to make incoherent measurements is by designing sensors that essentially correlate the signal with Gaussian white noise or binary independent, identically distributed random waveforms.

It has been shown that for a *k*-sparse signal (at most *k* non-zero expansion coefficients in the basis ψ), minimizing the L^1 norm reconstructs the signal exactly with overwhelming probability given that *m* measurements are made uniformly at random in Φ [15], where *m* is given by

$$m \geq \mu(\psi,\Phi) \cdot k \cdot \log_2 n \qquad (3.5)$$

This theorem emphasizes that it is the incoherence that allows sub-sampling of the signal for sparse reconstruction, the smaller the coherence μ and the fewer the number of samples needed to recover the signal. Compressive sampling takes this idea one step further by creating a measurement system for physical systems so that the real signal itself can be recorded in compressed form, bypassing the necessity to first capture digitally the full signal at high resolution and high data rate.

As an elementary example, consider the case of a one-dimensional signal that is sparse in the frequency domain. We assume a function expressible in the form of a sum of a small number of sinusoids,

$$f(t) = a_1 \sin(\omega_1 t) + a_2 \sin(\omega_2 t) + \ldots + a_n \sin(\omega_n t)$$

where the coefficients $\{a_i\}$ are the amplitudes and $\{\omega_i\}$ are the frequencies of the sinusoids. From the Shannon sampling theorem, the number of regular time domain samples of the signal required for perfect reconstruction will depend on the bandwidth of the signal and the frequency resolution desired. The sparse basis for this type of signal would be collections of sinusoids of the form $\sin(\omega_i t)$, where the frequencies span the bandwidth at the desired resolution. A suitable incoherent measurement system for this basis is to select random samples in the time domain, obtaining measurements $y_k = f(t_k)$, where the $\{t_k\}$ are selected randomly. The L^1 optimization problem is the constrained minimization over the variables $\{a_i\}$, expressed in the form

$$\min \sum_{i=1}^{N} |a_i|, \text{ subject to } y_k = \sum_{i=1}^{N} a_i \sin(\omega_i t_k)$$

For a numerical example, consider a signal consisting of two discrete sinusoids in it at frequencies 50 Hz and 100 Hz as shown in Fig. 3.5. We take 1024 samples of the signal in the time domain with a sampling frequency of 1024 Hz and take a 1024-point FFT to obtain the same number of frequency samples. For signal reconstruction, we only use a quarter of the 1024 samples in time domain chosen randomly. These random measurements are then used to find the minimum L^1 norm reconstruction of the signal. The L^1 recovery is exact as shown in the lower plots of Fig. 3.6 and Fig. 3.7 in the frequency domain and time domain respectively.

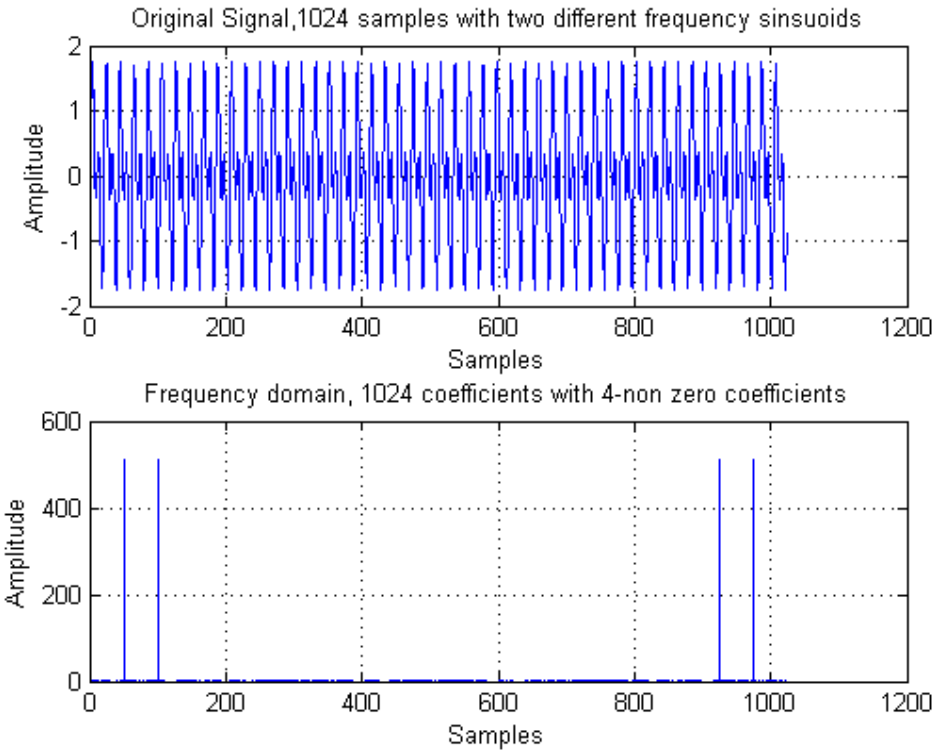

Fig. 3.5 Original signal in time and frequency domains.

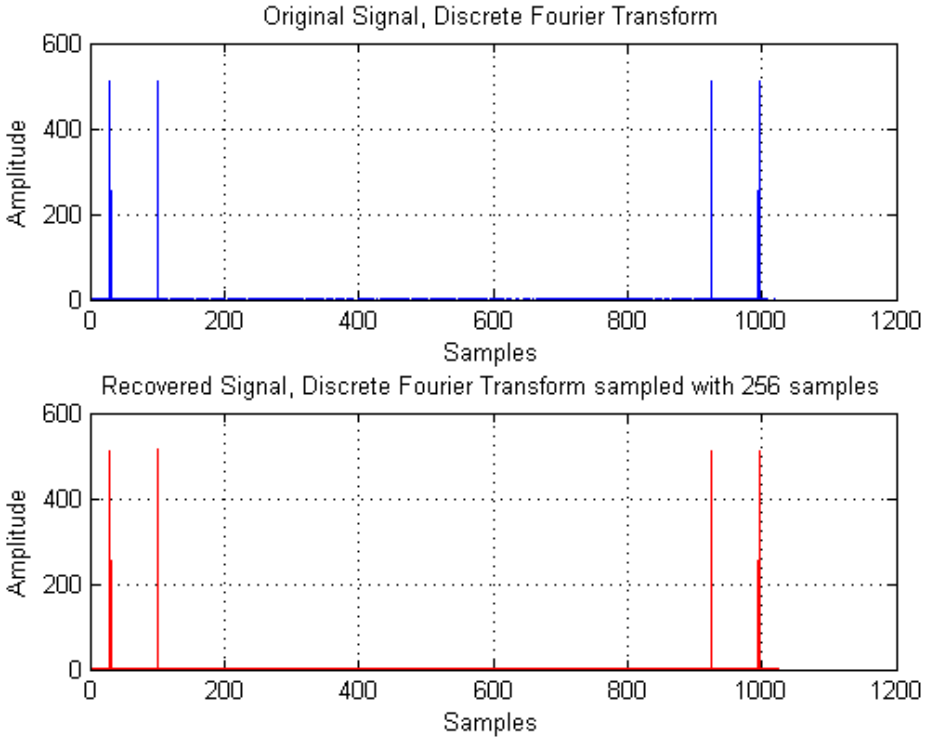

Fig. 3.6 Reconstructed signal in frequency domain.

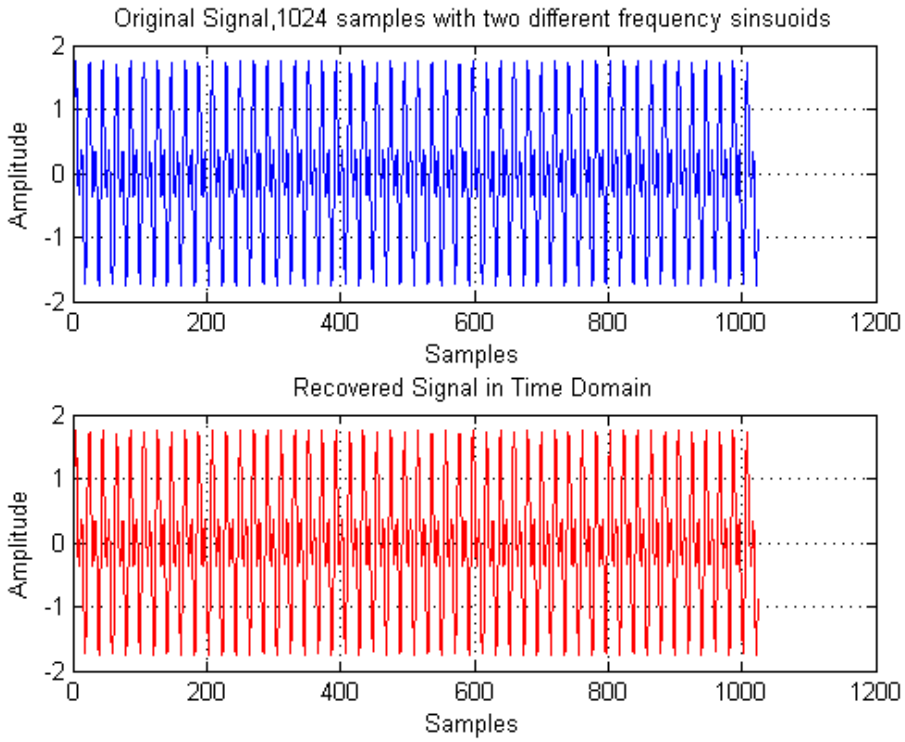

Fig. 3.7 Reconstructed signal in time domain.

Evaluation of Measurement Matrices

A key step in compressed sensing is the creation of measurement vectors Φ_1, Φ_2, ...,Φ_m for taking physical measurements on the signal in the form of inner products of the signal with the measurement vectors, $\mathbf{y}_k = \langle f, \Phi_k \rangle$. The measurement vectors are carefully designed to extract the maximum amount of information from a generic sparse vector in the given basis system. The optimization problem is replaced by a linearly constrained problem where the measurements of the signal must match the measurements on the representative solution.

One of the key tools for measuring incoherence and the orthonormal properties of the sensing matrix in compressive sensing is the notion of the *Restricted Isometry Property* (RIP). The sensing matrix Φ is said to have the RIP $(2k, \delta)$ if it preserves the Euclidean norm of sparse inputs within a factor of $(1\pm\delta)$ for a $2k$-sparse vector **x**. Mathematically, this

condition is shown in Eq. (3.6), which states that $\Phi\mathbf{x}$ must be greater than some constant times $\mathbf{x}$ when $\mathbf{x}$ is $2k$-sparse in order to ensure recovery of $\mathbf{x}$

$$(1-\delta)\mathbf{x}_2^2 \leq \mathbf{x}_2^2 \leq (1+\delta)\mathbf{x}_2^2 \tag{3.6}$$

One of the deep results in compressed sensing theory is that for a sparse signal of order k, only on the order of $k\cdot\log_2(n)$ measurement vectors are needed as seen in Eq. (3.5). In a successful compressive system, one designs for $k << n$. The measurement vectors, when organized into a $k\times n$, matrix, must satisfy the restricted isometry property. The Uniform Uncertainty Principle (UUP) of Candès and Tao [13] tells us that for δ sufficiently small, the constrained L^1 reconstruction is exact on sparse signals with high probability. Finding such measurement vectors is a challenge and forms an active area of research. One difficulty is that for practical problems the dimensions can be very high. The following choices of measurement matrices work with high probability:

- randomly choose m rows from an $n\times n$ orthogonal matrix and normalize the columns of the $m\times n$ matrix with respect to the L^2 norm, or
- randomly choose m unit vectors in the n-dimensional space and organize into the $m\times n$ matrix, or
- form a matrix with randomly chosen Gaussian entries.

Unfortunately, there is no deterministic approach to construct a measurement matrix guaranteed to have the required RIP, or to efficiently check if the RIP of a given measurement matrix has good recovery guarantees. Chandar [16] showed that binary matrices, in general, cannot achieve good performance with respect to the RIP and hence suffer inherent limitations. However, it has been shown that such matrices nevertheless satisfy a different form of the RIP called the RIP-p property, where the L^2 norm is replaced by the L^p norm ($1 \leq p \leq 1 + O(1)/\log_2 n$) [17]. Also, it has been pointed out in [18] that "RIP conditions are only sufficient and often fail to characterize all good measurement matrices." The construction of explicit matrices with an optimum number of measurements

for sparse reconstruction via L^1 minimization is an active area of research in compressed sensing [19].

Berinde and Indyk [20] consider matrices that are binary and sparse, i.e. they have only a fixed small number of ones *d* in each column, and all the other entries are equal to zero. This is the measurement structure we have assumed in this research and it is further explained in the next paragraph. Experimental results in [20] show that the minimum L^1 approach to recovery of sparse signals is as effective for L^1 recovery for binary sparse matrices as for random Gaussian or Fourier matrices, both in terms of necessary measurements and in terms of the recovery error. Another advantage of such matrices is their efficient update time in the solution algorithm, equal to the sparsity parameter *d*.

The measurement matrix for our multi-PRF system is formed by concatenating the individual binary Toeplitz matrices representing a single PRF as explained in Chapter 2. The concatenated measurement matrix has two important properties:

1. It is nonnegative.
2. The sum of the elements in each column is the same, and equals the number of PRFs.

The measurement matrix in the two-dimensional range-Doppler case also possesses these properties. L^1 recovery with measurement matrices that possess these two features has been considered in [19] and it was proved that if $A \in \mathbb{R}^{m \times n}$ is "a matrix with nonnegative entries and constant column sum, then for all nonnegative *k*-sparse $\mathbf{x}_0$, it holds that

$$\left\{\mathbf{x} \middle| A\mathbf{x} = A\mathbf{x}_0, \mathbf{x} \geq 0\right\} = \left\{\mathbf{x}_0\right\} \tag{3.7}$$

i.e. the condition for the success of L^1 recovery reduces to simply the condition for there being a "unique" vector in the constraint set". Exploiting this key fact, underdetermined systems representing radar measurements of the sparse target distribution in range or Doppler can be solved for the minimum L^1 norm solution to determine the unique unambiguous truth vector $\mathbf{x}$.

CHAPTER 4

SIMULATION SETUP AND RESULTS

In Chapter 2, we showed that the ambiguity resolution problem in the absence of errors can be modeled as a linear system of equations of the form $\mathbf{y}=A\mathbf{x}$ representing the multi-PRF measurements, and the solution to this system of equations gives the unambiguous truth vector $\mathbf{x}$ when $m_s \geq n$. However, the number of combined multi-PRF measurements m_s, which is the sum of the number of range bins in the unambiguous range of each PRF for the range-only case, is usually less than the number of range bins over which the radar's sensitivity allows detection of echo power received from the target. This results in an underdetermined system of equations. It was noted in Chapter 3 that an underdetermined system does not have a unique solution. Since the radar detection maps are sparse, we seek to solve the system for the sparsest solution in order to disambiguate the measurements. It was also shown in Chapter 3 that minimizing the L^1 norm of $\mathbf{x}$ with the constraint $\mathbf{y}=A\mathbf{x}$ gives a unique sparse solution to the underdetermined system of equations representing the multi-PRF measurements.

A large volume of work is dedicated to finding tractable methods for solving such sparse reconstruction problems. The idea is to relax a sparse recovery problem to a convex optimization problem, which can be further rendered as a linear program via a simple transformation of variables [21] and analyzed with all the available methods of linear programming. The idea of convex relaxation also became truly promising with the development of fast methods of linear programming in the past decade. The problem of finding a minimum L^1 norm solution to an underdetermined linear system is known as *basis pursuit*. Basis pursuit replaces an Np-hard problem with a linear optimization problem for which many off-the-shelf solvers exist. It has lately received a tremendous amount of attention in the literature. Several Matlab-based algorithms for L^1 minimization

have been proposed in the past few years and are publicly available to be used for the necessary computations. Reconstruction codes span a wide series of techniques that differ in terms of the underlying model and the methods employed to solve the problem. Several works also exist in the literature which attempt to provide comprehensive reviews on the performance of L^1 minimization algorithms [22], [23], [24]. In addition, various number of experiments are conducted to compare the performance of L^1 minimization algorithms in each individual paper that introduces new methods to the L^1 minimization problem.

In this chapter we will present some examples as a proof-of-concept demonstration of the proposed disambiguation technique, with the system of equations assumed to have no measurement errors. To solve these equality-constrained L^1 minimization problems we chose to use CVX, which is an open source Matlab-based modeling system for specifying and solving convex programs [25], [26]. We will first state the problem in terms of range only but all the results apply equally well in the range-Doppler case.

Simulated Ambiguity Resolution in Range

Consider a radar transmitting multiple-pulse packets with three different PRI values of 51 μs, 53 μs and 60 μs[4]. The unambiguous range for each PRI is $R_{ua} = c \times PRI/2$, which is 7.65 km, 7.95 km and 9 km respectively. If we assume a fast-time sampling rate of 1 μs, the size of one range bin would be 150 m and the above PRIs will have 51, 53 and 60 range bins respectively in the unambiguous range. Now suppose that the targets could be detected up to a maximum range of R_{max}= 90 km, or 600 range bins. Therefore, the truth vector $\mathbf{x} \in \mathcal{B}^{600}$ and the individual observation vectors for the three PRFs will have a dimension of 51, 53 and 60 respectively, i.e. the total number of unknowns n=600 and the total number of measurements m_s=51+53+60=164. Next, assuming a target sparsity of 1% of n, 6 targets

[4] These PRI values are taken from the set of eight PRIs obtained using evolutionary algorithms [28]

are randomly distributed in the 600 range bins. In this example, bin numbers 41, 126, 251, 333, 340 and 562 are selected as shown in Fig. 4.1.

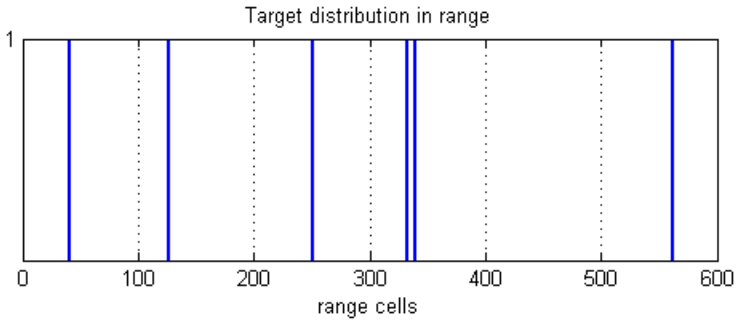

Fig. 4.1 Target distribution in range.

Since $R_{max}>R_{ua}$, the targets at a range R such that $R_{ua}<R<R_{max}$ will produce aliased measurements. The measurement matrices are constructed in the form of Toeplitz matrices shown in Eq. (2.7). The aliased measurements of the truth vector **x** made using the three PRFs represented by the Toeplitz matrices form the observation vectors $\mathbf{y}_1$, $\mathbf{y}_2$ and $\mathbf{y}_3$, which are related to **x** according to Eq. (2.10),

$$\begin{aligned} \mathbf{y}_1 &= T_{51,600}\mathbf{x} \\ \mathbf{y}_2 &= T_{53,600}\mathbf{x} \\ \mathbf{y}_3 &= T_{60,600}\mathbf{x}. \end{aligned} \tag{4.1}$$

Fig. 4.2 shows a plot of the three observation vectors. The dotted line shows the unambiguous range of the respective PRIs. All targets at a ranges beyond the unambiguous range for a given PRI can be seen to have folded over into the unambiguous range span bounded by the dotted line. Note that there are no collisions (two or more targets folding over into the same aliased range bin), false alarms or missed detections in this idealized example.

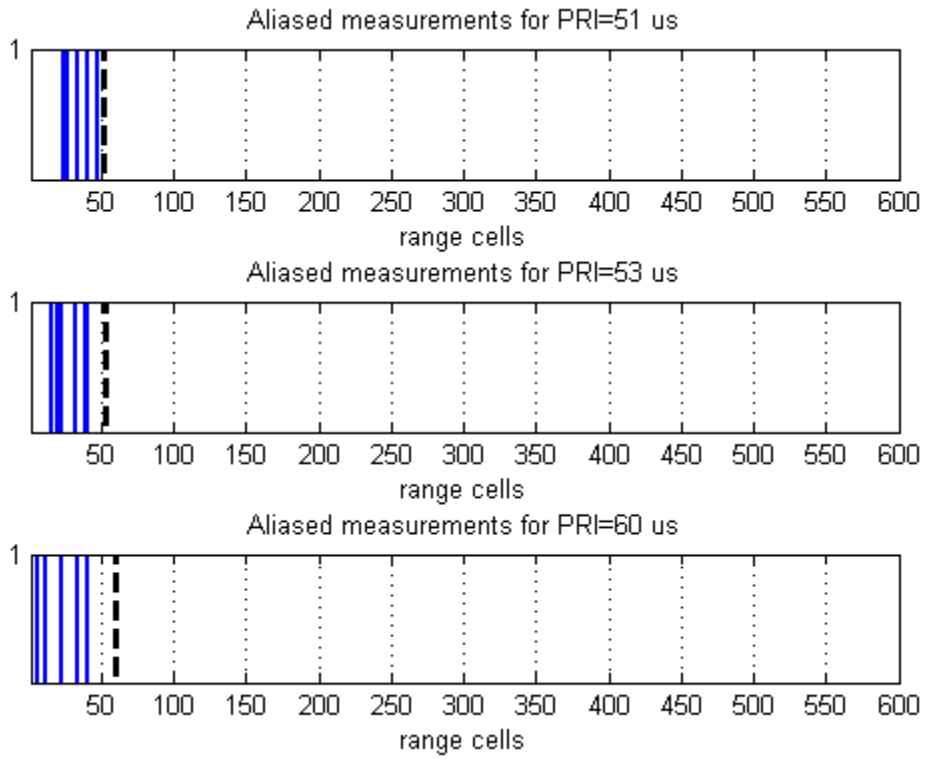

Fig. 4.2 Multi-PRF aliased measurements.

Our goal is to recover the unambiguous truth vector **x** in the form shown in Fig. 4.1. One final step before proceeding to solve the system is the concatenation of data to obtain one system of equations that represents all of the measured data as shown in Eq. (4.2). Once we have a single system of the form $\mathbf{y}=A\mathbf{x}$, we can attempt to solve the system for the sparsest solution. The complete system is

$$\mathbf{y} = \begin{bmatrix} \mathbf{y}_1 \\ \mathbf{y}_2 \\ \mathbf{y}_3 \end{bmatrix} = \begin{bmatrix} T_{51,600}\mathbf{x} \\ T_{53,600}\mathbf{x} \\ T_{60,600}\mathbf{x} \end{bmatrix} = A\mathbf{x} \qquad (4.2)$$

where

$$A = \begin{bmatrix} T_{51,600} \\ T_{53,600} \\ T_{60,600} \end{bmatrix}$$

CVX was used to find the minimum L^1 norm solution which leads to exact recovery of the truth vector **x** (Fig. 4.3 (a)) as shown in Fig. 4.3 (b). For the sake of comparison, the minimum L^2 norm solution is also computed and shown in Fig. 4.3 (c). It has a large number of non-zero components as the energy is spread throughout the target vector. The amplitudes at the target locations are, however, larger than the other non-zero elements in the solution vector. The L^2 norm of the residuals between the truth vector and the solutions obtained using different techniques is given in Table 4.1.

In addition to the above methods, Matlab itself has a built-in backslash operator which gives a "basic" sparse solution to an underdetermined system of equations. The '\' command invokes an algorithm with a host of powerful matrix solvers, the solver actually used depends upon the structure of the matrix *A*, i.e. whether the system is overdetermined or underdetermined, and includes checks on properties of *A*. By itself, the backslash operator deals only with the unconstrained system and the solution is never unique. The particular solution actually computed is determined by the QR factorization with column pivoting. In the case of overdetermined systems, the backslash operator gives the least squares solution. As stated earlier, an underdetermined system has either no solution (when it is inconsistent) or infinitely many. In the latter case, $A\backslash\mathbf{y}$ produces a basic solution, one with at most *r* nonzero elements, where *r* is the rank of A. If the system has no exact solution, i.e. it is inconsistent, then $A\backslash\mathbf{y}$ is a least squares solution [27]. The basic sparse solution of the above system obtained using the Matlab backslash function is shown in Fig. 4.3 (d). It completely fails to recover **x**, it. The number of non-zero elements in the backslash solution is 160, which is the same as the rank of the measurement matrix *A* in this example. It may be noted that with a higher m_s/n ratio, the backslash solution is not completely dissimilar to the truth vector as in this example. A more sparse solution is obtained when the number of measurements is increased.

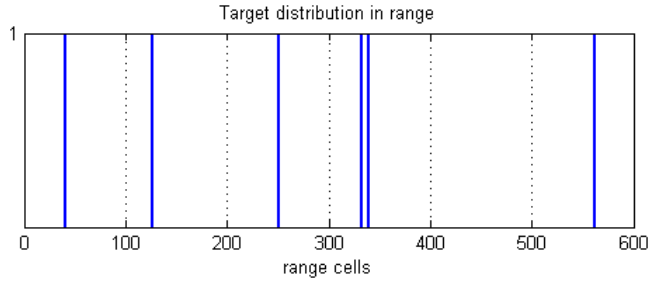

(a)

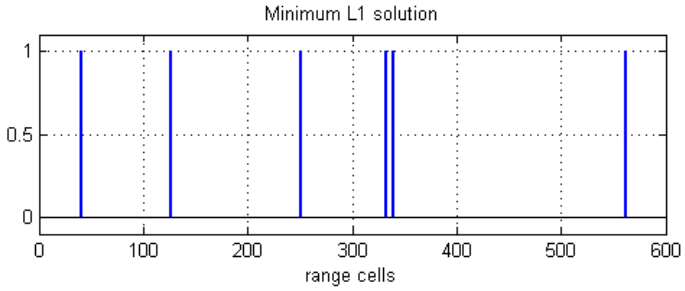

(b)

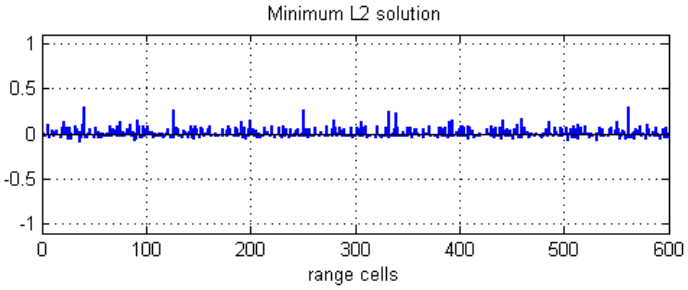

(c)

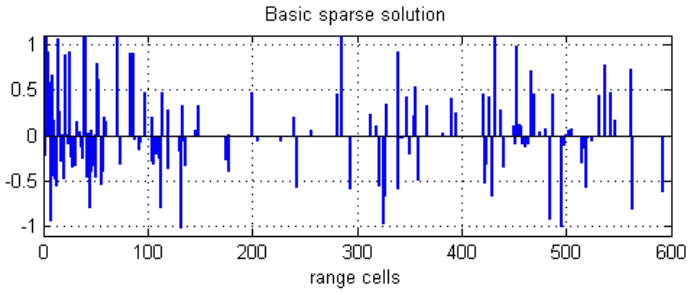

(d)

Fig. 4.3 Comparison of solutions to sample problem. (a) The truth vector **x,** (b) Minimum L^1 solution, (c) Minimum L^2 solution, and (d) Matlab backslash solution.

TABLE 4.1 Comparison of the residuals for different solutions.

Solutions	**Residuals (L^2 norm)**
Minimum L^1	2.4471×10^{-13}
Minimum L^2	2.1032
Backslash	6.2094

The above example demonstrates that the unique sparse solution to the underdetermined system of equations representing the multi-PRF measurements can be obtained using the L^1 minimization technique, in accordance with Eq. (3.5). The simulations were carried out with hundreds of different target distributions and similar results were obtained. In all cases, the minimum L^1 solution was correct, the minimum L^2 solution had large residuals but strongest at correct locations and the backslash solution failed to completely recover the truth vector **x**.

Simulated Ambiguity Resolution in Range and Doppler

The L^1 minimization approach presented above can be easily extended to account for both range and Doppler ambiguities. This is done by vectorizing the two dimensional range-Doppler detection matrix and then solving the system of equations in the same way as in the case of one dimensional range ambiguities as discussed in Chapter 2. Vectorization, however, greatly increases the size of the data vectors and can result in memory problems while running simulations on a standard laptop computer like that used for this research. To avoid memory problems, we used the sparse representation feature in our simulations that generates matrices in the Matlab sparse storage organization.

As a proof-of-concept for range and Doppler ambiguity resolution, the new technique was tested using radar parameters based on an X-band airborne pulse Doppler medium PRF mode radar (see [28], Table I). Assuming a sparsity of 0.01% of *n*, 20 targets were randomly distributed in the truth vector **x**, which consists of a total of 200,000 range-

Doppler bins. Some random target locations may fall in range or Doppler blind zones for a particular PRI set, but for this proof-of-concept demonstration it has been assumed that they are nonetheless detected. Extensions to account for missed detections due to blind zones are presented in Chapter 5.

We used the medium PRF set of eight PRFs found using evolutionary algorithms for optimum blind zone performance with PRIs of {51, 53, 60, 63, 67, 84, 89, 93} μs [28]. From the PRF set and other radar parameters, we can calculate the number of range cells in the unambiguous range for each PRF, as well as the number of velocity cells in the unambiguous velocity distribution (0, PRF) of each PRF. Since a sampling time of 1μs is assumed in the radar parameters, the number of unambiguous range cells in each PRF is **R** = {51, 53, 60, 63, 67, 84, 89, 93}. Assuming R_{max}=150 km, the total number of unaliased range cells is 1000. The unambiguous velocity V_{ua} for each PRF can be found using the relation $V_{ua}=2(\lambda/PRF)$. The wavelength λ corresponds to the operating frequency of radar which is assumed to be 10 GHz so that λ=3 cm. In order to determine the number of velocity cells in the unambiguous velocity interval of each PRF, the Doppler resolution has to be specified and used to find the velocity resolution of a cell. The unambiguous velocity interval is then divided by the velocity resolution to get the number of unambiguous velocity cells for each PRF. A Doppler resolution of 100 Hz is specified in [28] which corresponds to a velocity resolution of 1.5 m/s. We now have all the information to determine the number of velocity cells in the unambiguous velocity interval of each PRF. These are **V** = {196, 189, 167, 159, 149, 119, 112, 108} respectively for our eight PRF set. Finally, the maximum range of target velocities expected to be encountered by the radar (±150 m/s from [28]) is divided by the velocity resolution to get the number of velocity cells over which the targets might be detected, i.e. 300/1.5 = 200 velocity cells.

Once we have all the range and Doppler detection data, it can be plotted in the form of a 2-D range-Doppler detection map. Fig. 4.4 shows the actual target distribution of eight targets in the 2-D range-Doppler map. For visibility purposes, targets have been magnified

from their actual girth of one bin to the diamond shapes in Figs. 4.4. After the range-Doppler matrix is vectorized, m_s is now given by the sum of the number of cells in the unambiguous range times the number of velocity cells in the unambiguous velocity measurements for each PRF, i.e. $m_s = \sum_{i=1}^{8} R_i V_i = 80041$. The total number of range-Doppler bins n becomes the product of the number of unaliased range bins and the number of unaliased velocity cells (1000×200). Consequently, the m_s/n ratio in this case is 80041/200000 = 0.4 which means the total number of measurements is 40% of the total number of unknowns.

To demonstrate the ambiguity in the measured data, the aliased measurements made with three of the set of eight different PRIs, {51, 63, 93} μs, are shown in Fig. 4.5 (a), (b) and (c). The dotted rectangle indicates the extent of the range-Doppler cells covered with a single PRF measurement, i.e. all the measurements will be folded over in the area bounded by this rectangle. This data is vectorized and a system of linear equations constructed as described in Chapter 2. The minimum L^1 solution was generated using CVX and converted back to matrix form. The result is shown in Fig. 4.6 overlaid on the original target distribution. It can be seen that the L^1 minimization accurately resolves all target ambiguities in both range and Doppler in the absence of measurement errors and collisions. As with the range-only case, simulations were carried out with many different parameter sets and the L^1 recovery was always successful in the absence of errors.

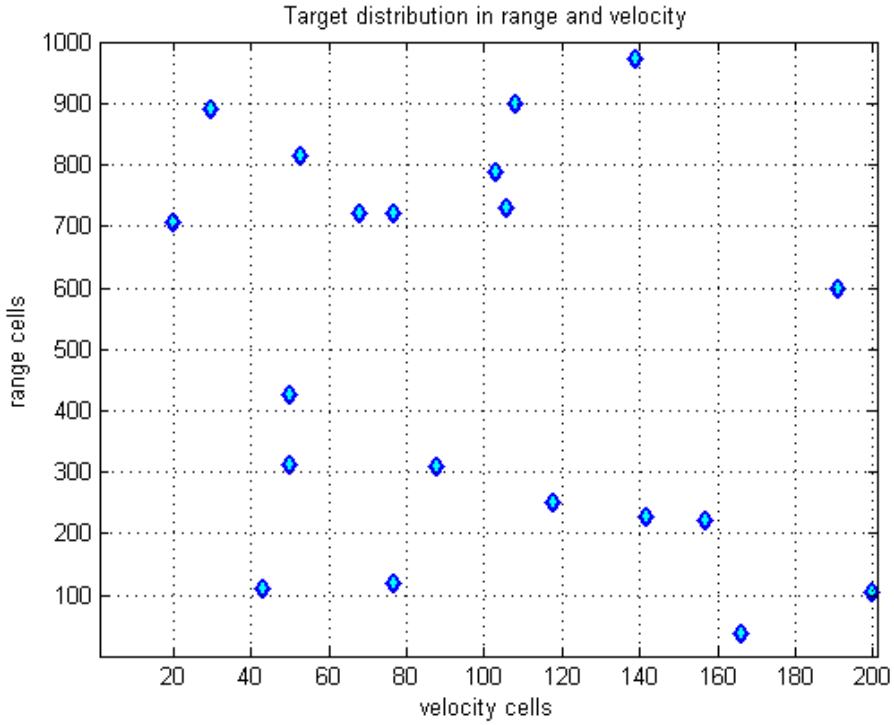

Fig. 4.4 Actual target distribution (range and Doppler).

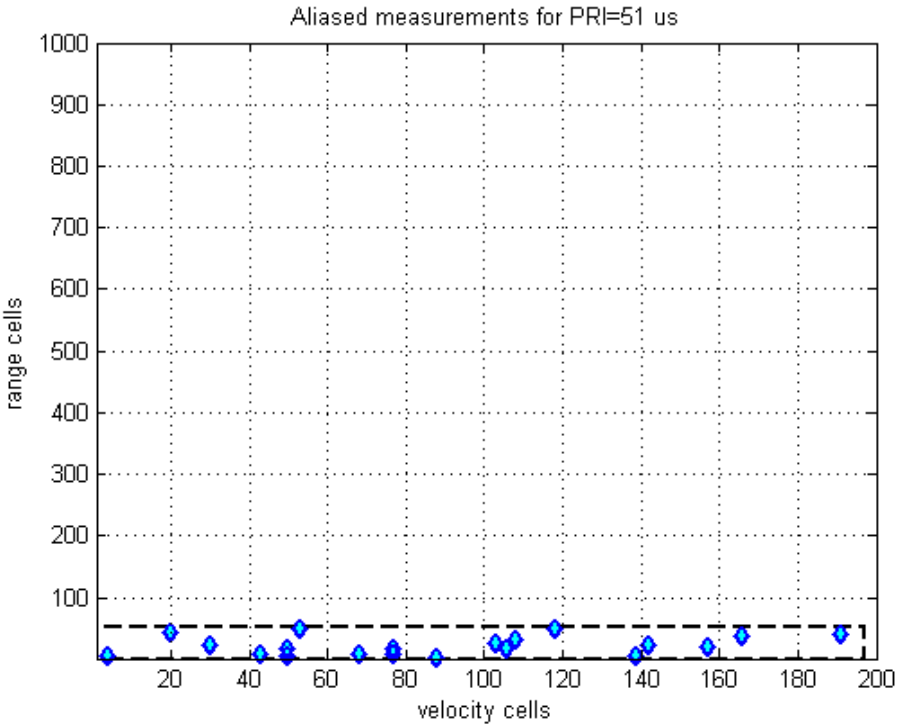

(a)

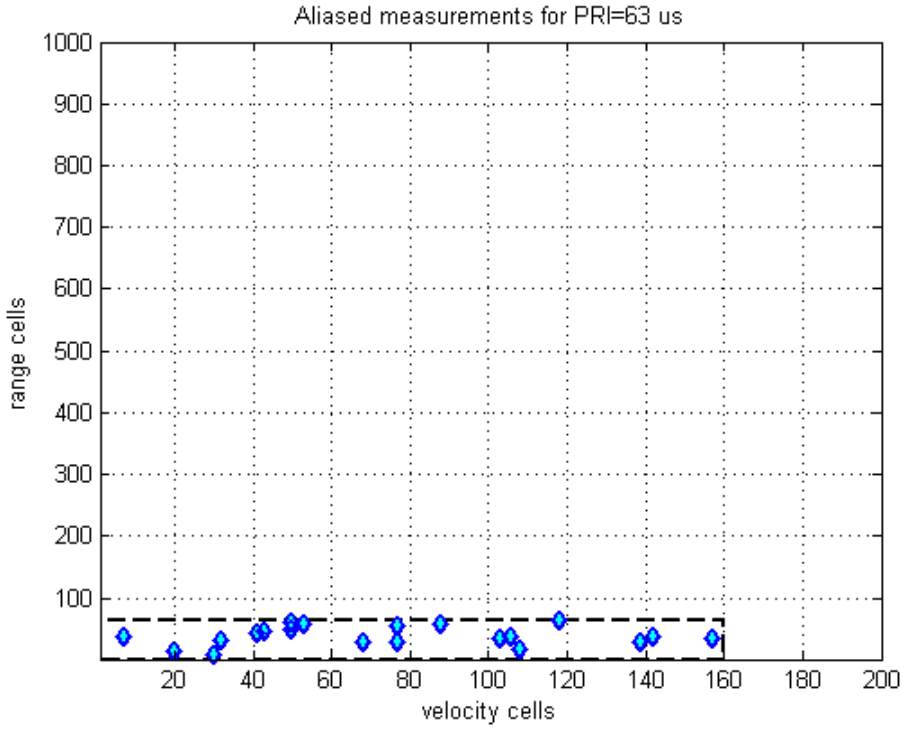

(b)

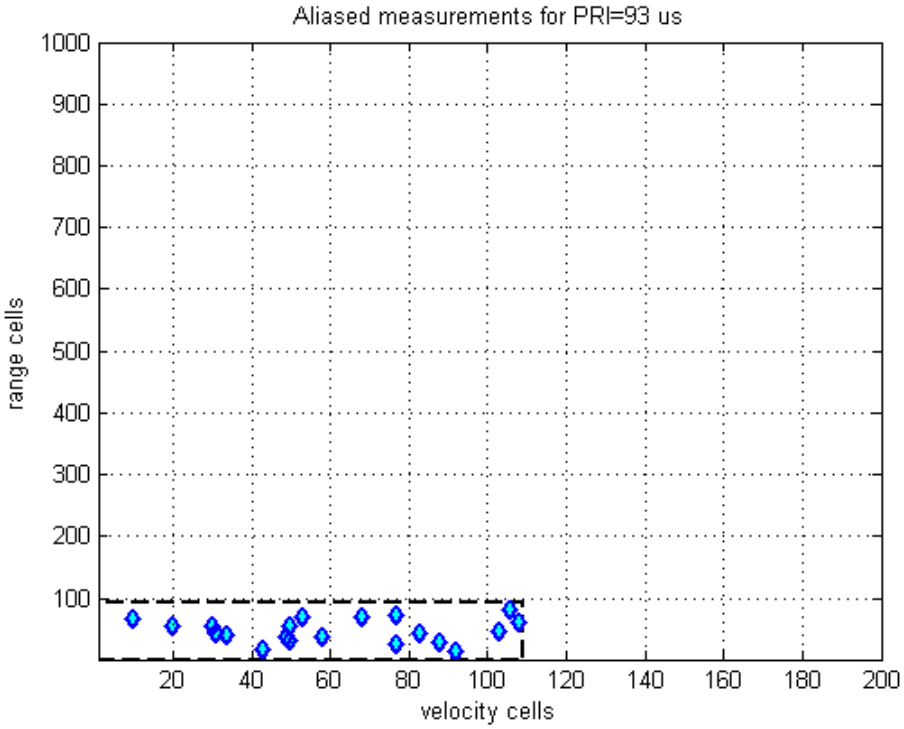

(c)

Fig. 4.5 Aliased range-Doppler measurements. (a) PRI = 51 μs, (b) PRI = 63 μs and (c) PRI = 93 μs.

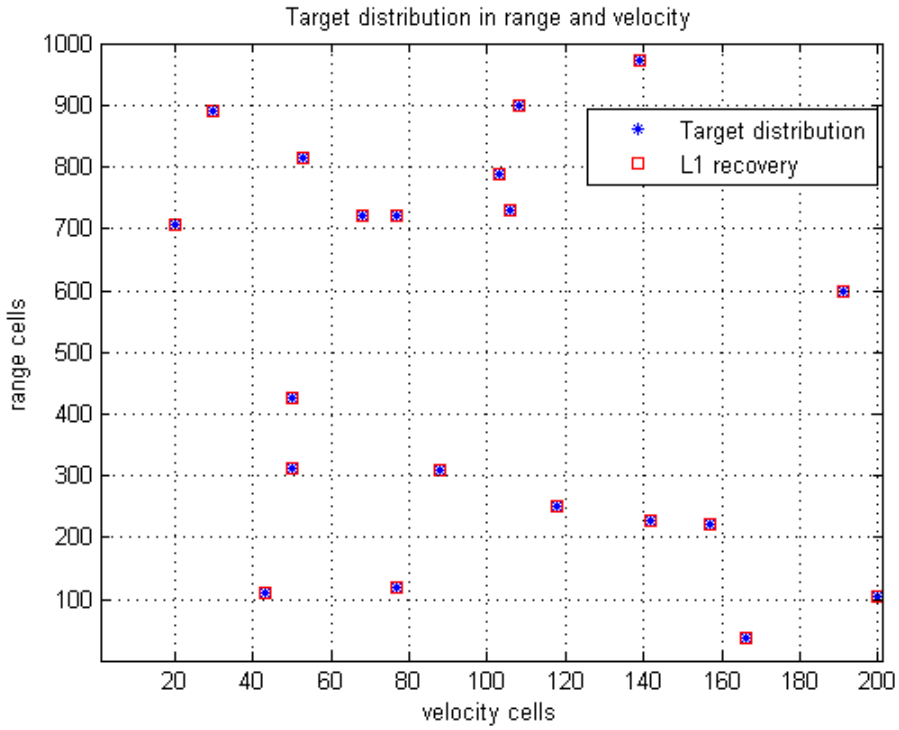

Fig. 4.6 L^1 recovery of the unambiguous target distribution.

Required Number of Measurements

It is important to note that the recovery is not exact if the number of measurements is insufficient for a conclusive determination of all target locations. In that case, the target energy starts spreading across multiple candidate range or range-Doppler cells in the solution vector that could account for the target location in the absence of a sufficient number of measurements for a definitive solution. For example, the range ambiguity example presented earlier was solved using three PRFs (51, 53 and 60 range bins in the unambiguous range) with the total number of measurements m_s=164 and n=600. If we attempt to solve the same problem with the same target distribution in the truth vector **x** using the first two PRFs only, m_s will then be 51+53=104. The minimum L^1 solution in this case is shown in Fig. 4.7 along with the original target distribution. It can be seen that only two out of the six targets are fully resolved with an amplitude of 1 in the solution vector. The remaining four targets have their energies split among all the potential locations

in the solution vector that are consistent with the measurements made using two PRFs. For example, the target at range bin 200 splits into range bins 200 and 251 in the solution vector which are separated by the range bins in the first PRI (51 range bins). Similarly, the target at range bin 340 splits into range bins 340 and 391. It may be noted that the L^1 norm of the solution vector is approximately the same as the L^1 norm of the truth vector **x**.

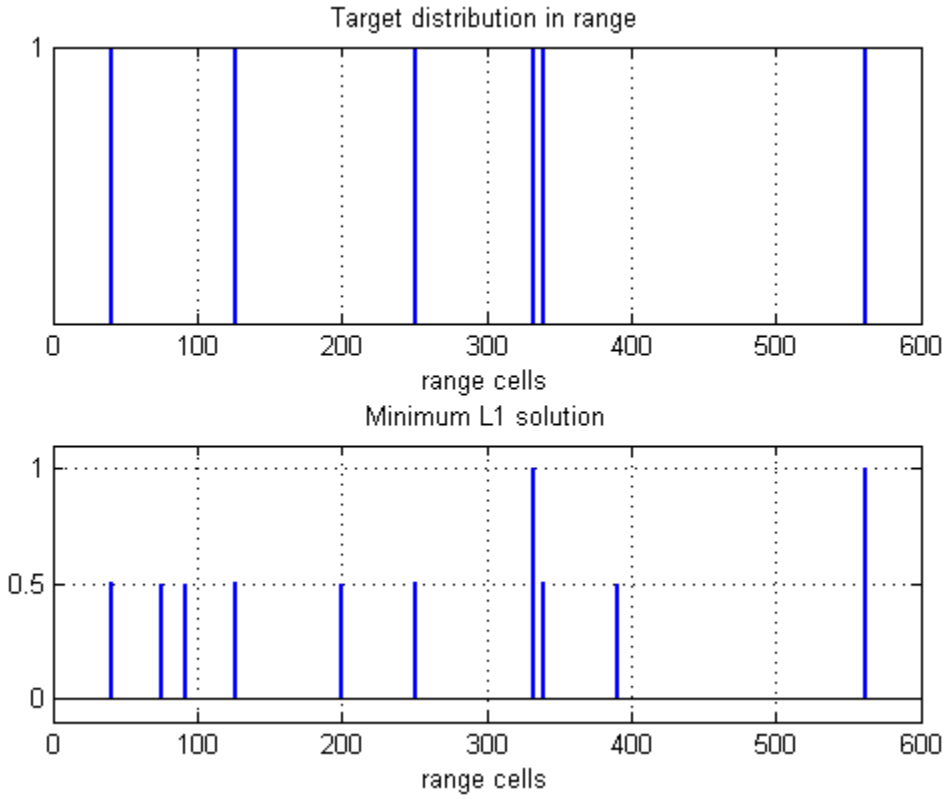

Fig. 4.7 L^1 recovery in case of insufficient measurements.

It was pointed out in Chapter 3 that for a signal of sparsity k, the compressed sensing theory requires a number of measurements on the order of $(k \cdot \log_2 n)$ for the L^1 recovery. In our multi-PRF measurements, we see that the number of measurements required for the exact recovery of a k-sparse vector $\mathbf{x} \in \mathcal{B}^n$ not only depends on n and k, but also the number of PRFs N_{PRF}. To investigate the effect of changing these variables and the number of measurements m_s on the recovery of the truth vector **x**, we followed the approach presented in [18] and [19], where k is taken to be a small fraction of n and the number of

measurements is also a fraction of n. In an effort to determine the required number of measurements for the correct recovery of $\mathbf{x} \in \mathcal{B}^n$, Monte Carlo simulations were carried out with the number of measurements m_s in the range from 5% to 50% of n for a given set of n, k and N_{PRF}. With 500 trials of different target distributions for each value of m_s and the number of times the correct solution is obtained, a probability of correct solution P_c can be defined. We define a "correct" solution as one having a normalized L^2 norm less than or equal to 10^{-3} for the difference between the actual truth vector $\mathbf{x}$ and the solution vector $\mathbf{x}^*$,

$$\frac{\left\|\mathbf{x}-\mathbf{x}^*\right\|_2}{\left\|\mathbf{x}\right\|} \leq 10^{-3}$$

which is a very conservative measure in the sense that for a reasonably large n, targets are still discernible in the solution vector even when the residual norm is of the order of 10^{-1}.

The Monte Carlo simulations were conducted for the range-only case assuming n=1000 for the truth vector $\mathbf{x}$. Considering a three-PRF protocol first, the total number of measurements m_s was varied from 5% of n to 50% of n and the trials were carried out for three different values of target sparsity k, k=10, 15, and 25 (1 to 2.5% of n). Based on the outcome of 500 trials, P_c was computed as the number of times a correct solution was obtained over the total number of trials for each value of m_s.

Fig. 4.8 shows P_c plotted against m_s/n for k=10, 15, and 25. It is observed that if k is a larger percentage of n (denser target environment), then the required m_s is also a larger percentage of n provided the number of PRFs remains constant. In terms of radar measurements, larger m_s with a fixed number of PRFs is equivalent to having longer PRIs. This is consistent with the compressed sensing requirement of ($k \cdot \log_2 n$) measurements which requires an m_s/n ratio of approximately 0.10, 0.15 and 0.25 for k=10, 15, and 25 respectively. For example, with k=10 and n=1000, m_s should be on the order of $10 \cdot \log_2(1000) \approx 100$, so that m_s/n=1000/100=0.10. We see that P_c is in the range of 80 to 90% for the three values of k with a minimum m_s/n ratio of approximately 0.10, 0.15 and

0.25 respectively. P_c can be further improved for a fixed m_s/n ratio by increasing the number of PRFs as discussed in the following paragraph.

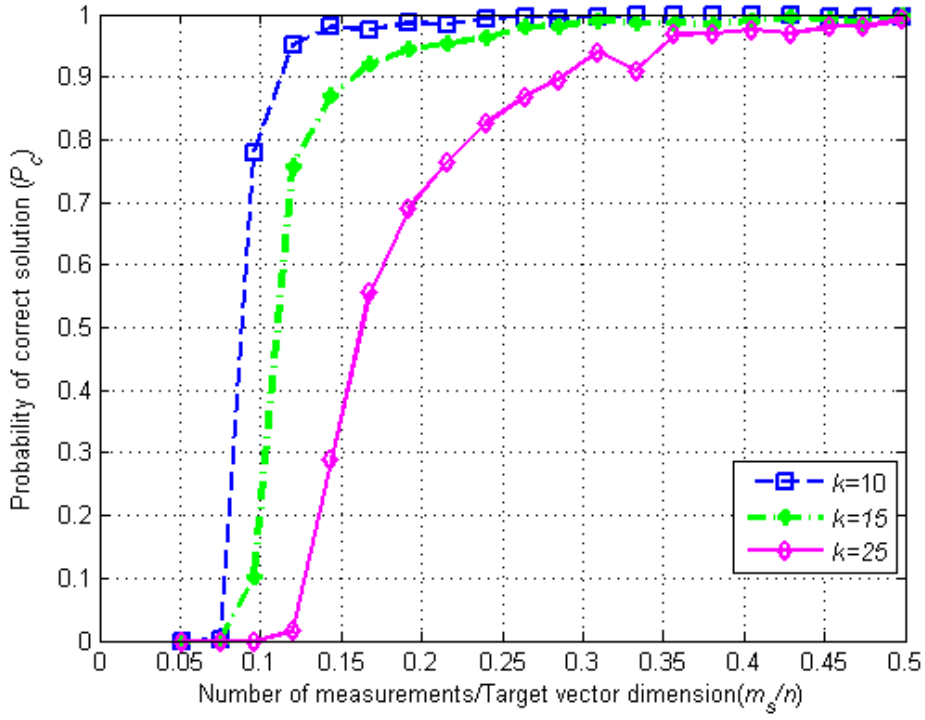

Fig. 4.8 Effect of varying target sparsity (n=1000, #PRFs =3).

The next set of Monte Carlo simulations was conducted with the sparsity fixed at k=10 and the number of measurements in the range of 5 to 50% of n. These measurements were split into three different number of PRFs, i.e. N_{PRF}=3, 4 and 5. Again, the probability of obtaining the correct solution P_c was computed for each value of m_s and plotted against m_s/n for N_{PRF}=3, 4 and 5 as shown in Fig. 4.9. It is observed that P_c increases to approximately 97.6% for the minimum m_s/n ratio of 0.10 when the N_{PRF} is increased from 3 to 4, and it is approximately 99.6% when N_{PRF} is further increased from 4 to 5. The experiment was also repeated with even higher numbers of PRFs (6, 7 and 8) but no further improvement was observed. This indicates that the required m_s/n ratio, and therefore the required number of measurements m_s, can be improved by increasing the number of PRFs but only to a degree. Fig. 4.8 and Fig. 4.9 together suggest having as many PRFs as allowed

by the system requirements and constraints, and then setting the PRIs accordingly taking into account the minimum number of measurements required for the particular number of PRFs chosen for the system. We will see in Chapter 5 that factors like blind zone performance, clutter rejection and target illumination times are also important in choosing the number of PRFs and the PRF values for real-world radar measurements [29].

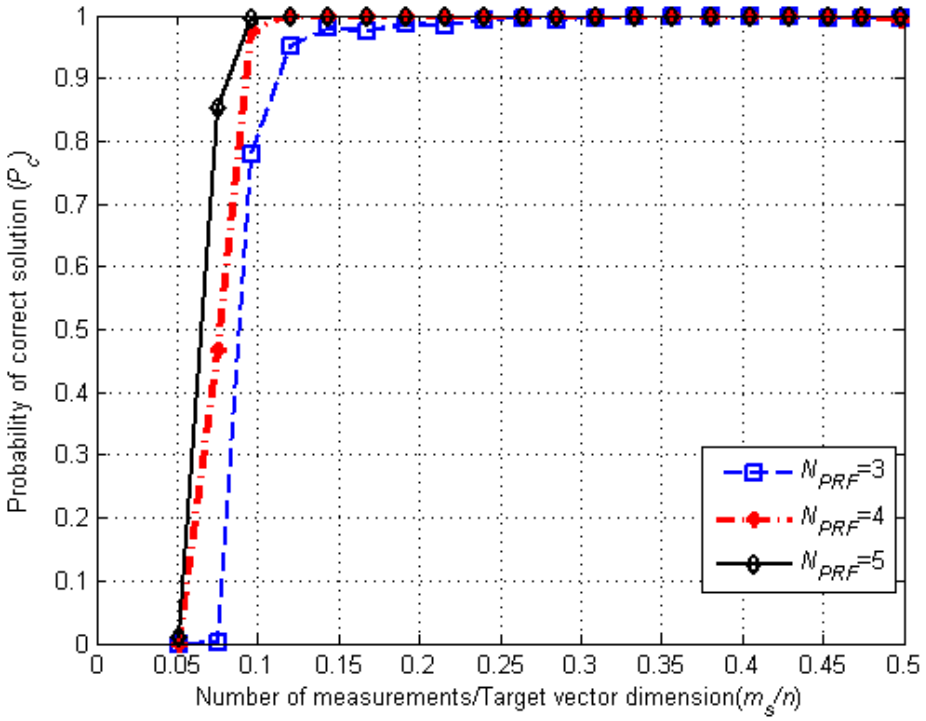

Fig. 4.9 Effect of varying the number of PRFs (n=1000, k=10).

CHAPTER 5

AMBIGUITY RESOLUTION IN THE PRESENCE OF ERRORS

In Chapter 4, ambiguity resolution capability using L^1 minimization was successfully simulated assuming no errors in the measurement. In this chapter, the behavior of the technique will be investigated in the presence of real-world effects in the radar measurements and detection process. Below we give a short account of the different sources of error and how they are accounted for in the mathematical model.

False Alarms and Missed Detections

In Chapter 2, we explained the statistical threshold detection process carried out in radars along with measures of quality like probability of false alarm and probability of missed detection. Threshold detection is carried out for each data bin and a false alarm occurs if a threshold crossing occurs as the result of interference only when no target is present. In this case, a bin has a "1" where there should be a "0". A missed detection occurs in a data bin when the target is present but the echo signal coupled with interference fails to cross the threshold. In this case, a bin has a "0" where there should be a "1". Since the detection tests are carried out for each PRF measurement and false alarms and missed detections are random occurrences, it follows that the erroneous false alarm detections made with one PRF measurement will not be consistent with either the false or actual target detections observed in other PRF measurements. Similarly, the missed detection of a target can occur in one or more of the PRF measurements, which will be then inconsistent with other PRF measurements in which the target is detected. The resulting underdetermined system of equations is, therefore, *inconsistent* when false alarms and missed detections occur.

False alarms and missed detections can be modeled by adding an error vector $\mathbf{e}_i$ to the observation vector $\mathbf{y}_i$ in Eq. (2.9). The modified set of equations can be written as:

$$\begin{aligned} \mathbf{y_1} &= T_{m_1,n}\mathbf{x} + \mathbf{e}_1 \\ \mathbf{y_2} &= T_{m_2,n}\mathbf{x} + \mathbf{e}_2 \\ \mathbf{y_3} &= T_{m_3,n}\mathbf{x} + \mathbf{e}_3. \end{aligned} \tag{5.1}$$

The error vector takes on values of +1 or -1 for false alarms and missed detections respectively in the bins where errors occur and zeros elsewhere. The number of non-zero error terms in the error vector depends on the dimensionality of the problem, the probability of false alarm P_{FA}, and the probability of missed detection P_M (identified as β in Table 2.1 of Chapter 2). As discussed in Chapter 2, the Neyman Pearson detection criterion dictates maximizing P_D subject to a fixed value of P_{FA} set according to system requirements. False alarm probabilities between 10^{-4} and 10^{-6} and detection probabilities of 0.7 to 0.9 or higher are typical in most radar systems. As shown earlier, the probability of detection is related to the probability of missed detection as $P_D = 1-\beta$. The typical missed detection probabilities are therefore 0.1 to 0.3. In our simulations, we will assume a false alarm probability of 10^{-4} or higher and a missed detection probability of 0.1 or lower depending on the problem size. On the average, these probabilities translate to having one false alarm every 10,000 detection tests, and a missed detection every 10 target detections.

Collisions

In Chapter 2, we explained the *collision* phenomenon which refers to the inability of radar to distinguish between echoes from two (or more) targets at the same apparent range but different unaliased ranges. This results in the "missed detection" of one of the two targets. To model collisions, we restrict the observation vector to have binary values only by clipping any values greater than 1, which represent the folding over of more than one targets into the same range bin, to a value of 1. This process accurately models the fact

that a detection indicates only the presence of a signal in addition to the noise, but does not indicate the number of targets giving rise to that signal.

Owing to the sparsity of detection maps, collisions are also a rare occurrence in radar measurements. To estimate the probability of occurrence of a collision, we conducted an experiment creating a range-Doppler matrix with a total of n=100,000 range-Doppler bins. Assuming a target sparsity of 0.01% of n, 10 targets were randomly distributed in the range-Doppler matrix and aliased measurements were made with the eight PRFs obtained using evolutionary algorithms [28]. Monte Carlo simulations were carried out and the observation vector **y** in each simulation was examined for any non-binary values that would show the "collisions" in target detection. In 3000 trials, 145 out of a total number of 30,000 detections were seen to have aliased to the same range-Doppler bin, which gives a collision probability value of $P_{col} = 4.8\times10^{-3}$. In addition to target distribution, the collision probability also depends on the ratios R_{max}/R_{ua} and V_{max}/V_{ua}; the higher these ratios, the greater the probability of collisions. It may be noted that the collisions caused by more than two targets aliasing to the same cell are very rare. In our experiment where 145 collisions were observed in 10,000 detections, all 145 were caused by the aliasing of two targets while none were seen to be produced by the aliasing of three targets into the same cell.

Blind Zones

Chapter 1 gave a short account of the effect of blind zones on the measurements. If a target happens to be at a range such that the echo is received during one of the range blind zone intervals represented by the horizontal black stripes in Fig. 1.6 it will go undetected. Similarly, if a target is moving with a velocity such that the return signal is received in one of the Doppler blind zone intervals represented by vertical stripes, it will not be detected. It must be kept in mind that the each PRF is characterized by different regions of blind ranges and velocities.

In our simulation protocol, the targets are randomly distributed in the range-Doppler matrix when setting up the problem. If a target location happens to be in a blind cell for a given PRF, it must be modeled as undetected in the measurements made with that PRF. Thus, missed detections can be caused by incorrect decisions in the detection process, collisions and blind zone effects. We can, therefore, state that the collisions and blind zone effects are equivalent to missed detections and can be modeled in the same way using Eq. (5.1).

Basis Pursuit Denoising

As noted earlier, the addition of false alarms and missed detections in the mathematical model renders the underdetermined system of equations representing the multi-PRF measurements *inconsistent*. Therefore, the system must be solved for an approximate solution which minimizes the errors. The L^1 minimization of the underdetermined system of equations with an added constraint of minimizing the errors is known as *basis pursuit denoising*. Just like basis pursuit, several algorithms exist for solving the basis pursuit denoising problem. One of the implementations minimizes the L^1 norm of **x** under the constraint of minimizing the L^2 norm of the error (**y**-*A***x**).

$$\mathbf{x} = \min\left\{\|\mathbf{x}\|_1\right\} \text{ subject to } \|A\mathbf{x} - \mathbf{y}\|_2 \leq \varepsilon, \tag{5.2}$$

where ε is a user-specified estimate of the standard deviation of the errors in the system. Another formulation for basis pursuit denoising is the L^1 regularized least squares problem defined by

$$\mathrm{x} = \min\left\{\|A\mathrm{x} - \mathrm{y}\|_2 + \lambda\|x\|_1\right\}, \tag{5.3}$$

where $\lambda \geq 0$ is a regularization parameter that also governs the sparsity of the solution. Sparse solutions are obtained for sufficiently large values of λ [30], [31]**.** A Matlab-based

solver *l1_ls* [32] uses the interior point method[5] to solve the L^1 regularized least squares problem. This code handles large sparse problems efficiently and has a variant that solves for strictly non-negative **x**, making it particularly well-suited to our application.

A more sparse solution to the basis pursuit denoising problem can be obtained by minimizing the L^1 norm of **x** with the constraint of minimizing the L^1 norm of the error (**y**-*A***x**).

$$\mathbf{x} = \min\left\{\|\mathbf{x}\|_1\right\} \text{ subject to } \|\mathrm{A}\mathbf{x} - \mathbf{y}\|_1 \le \rho, \tag{5.4}$$

where ρ depends on the standard deviation of the errors and sets the upper bound on the L^1 norm of the residuals. This approach can be implemented in the simulations using CVX [25], [26].

False Alarms Simulations

We will demonstrate the effect of errors in the measurements by first setting up an example in range only. Consider the same example that was presented in Chapter 4 for simulating range ambiguity resolution with six targets randomly distributed in range as shown in Fig. 5.1. The only change in data that we will make is the addition of a false alarm in each of the measurements. Since the truth vector $\mathbf{x} \in \mathcal{B}^{600}$, the number of detection decisions made will be 600 for each PRF. A false alarm probability of 10^{-4} implies a false alarm rate of one per 10,000 detections on the average. For this simulation, we will nonetheless add one false alarm in each PRF measurement at a random location. The implied P_{FA} is then 1.6×10^{-3}. The false alarms added to the aliased measurements are shown as an extra measurement in red in addition to the six target detections in Fig. 5.2 (a), (b) and (c). Note that since the maximum unambiguous range consists of 60 range bins

[5] An interior point method is a programming method to solve linear and nonlinear convex optimization problems. It achieves optimization by going through the middle of the solid defined by the problem rather than around its surface. For more details, the reader is referred to [33].

corresponding to PRI = 60 μs, the horizontal scales of Fig. 5.2 (a), (b) and (c) have been reduced to show 75 range bins each to improve visibility of the aliased measurements. The same scale will be used for all plots of aliased measurements shown henceforth.

The concatenated system is then solved for the minimum L^1 norm solution under the two constraints stated earlier, minimizing the error in the L^2 sense and L^1 sense. Figure 5.3 (b) plots the solution obtained solving for the minimum L^1 norm $\mathbf{x}$ with minimum L^1 norm of the residuals as shown in Eq. (5.4). Figure 5.3 (c) shows the result of solving with the L^1 regularized least squares method given in Eq. (5.3). The average value of the residuals in the minimum L^1 residuals solution is 0.0183, the peak value is 1 (at the false alarm locations) and the L^2 norm of the error between the solution vector and truth vector is approximately 8.67×10^{-11}. On the other hand, the average value of residuals in the L^1 regularized least squares solutions is 0.0216, the peak value is 0.1673 and the L^2 norm of the error between the solution vector and truth vector is 0.6908. While the disambiguated target locations are recovered in both solutions, it can be seen that minimizing the L^1 residuals gives a more sparse solution than the L^1 regularized least squares. The latter produces errors distributed throughout the solution vector at all possible locations that could account for the inconsistent false alarms added in the measurements. At the same time, the amplitude degrades somewhat for some of the actual target detections in the L^1 regularized least squares solution as the energy divides into other potential target locations due to the inconsistent measurements.

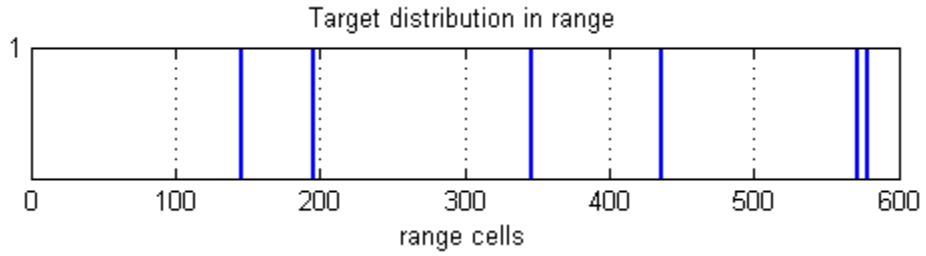

Fig. 5.1 Unaliased target distribution for false alarm simulation.

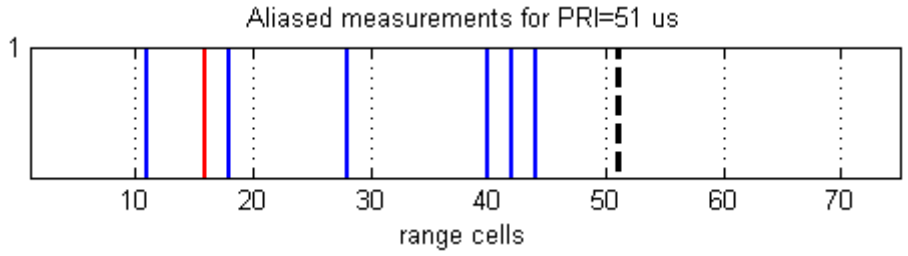

(a)

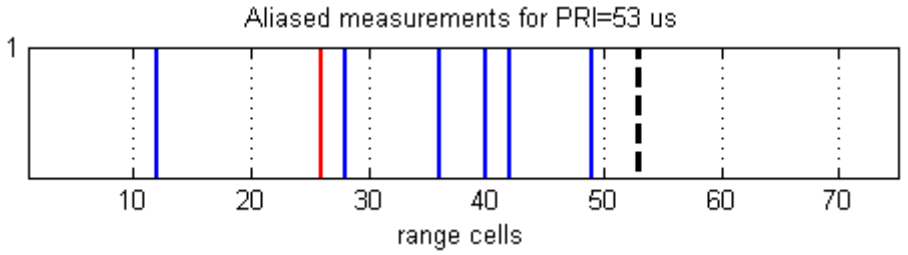

(b)

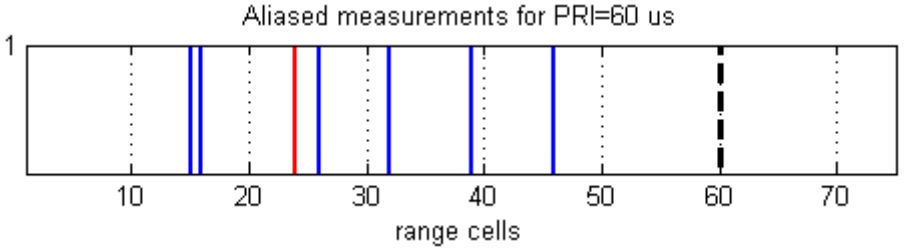

(c)

Fig. 5.2 Multi-PRF aliased measurements with false alarms shown in red. (a) PRI = 51 μs, (b) PRI = 53 μs and (c) PRI = 60 μs.

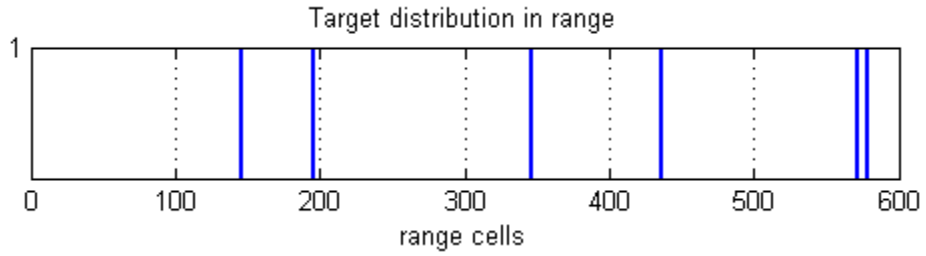

(a)

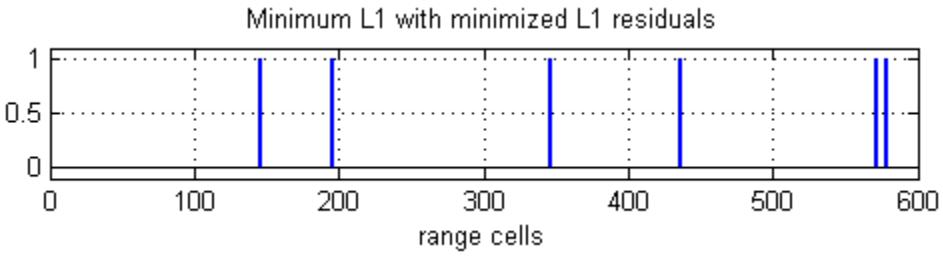

(b)

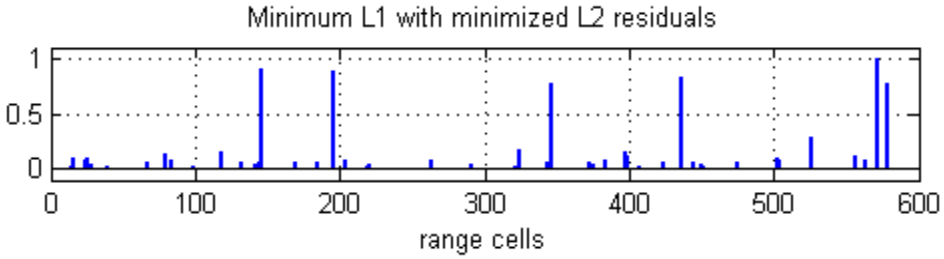

(c)

Fig. 5.3 Comparison of solutions to sample false alarm problem. (a) Target distribution, (b) Minimum L^1 residuals solution and (c) Minimum L^2 residuals solution.

Multiple trials of the same experiment with different target distributions were conducted and similar results were obtained. This spreading of target energy in the solution vector can be demonstrated by considering a simplified system of the form $\mathbf{y}=A\mathbf{x}+\mathbf{e}$ shown below with one false alarm.

$$\begin{bmatrix}0\\1\\0\\1\end{bmatrix}=\begin{bmatrix}1&0&0&0&1&0&0&0&1&0&0&0\\0&1&0&0&0&1&0&0&0&1&0&0\\0&0&1&0&0&0&1&0&0&0&1&0\\0&0&0&1&0&0&0&1&0&0&0&1\end{bmatrix}\begin{bmatrix}0\\0\\0\\0\\0\\0\\0\\0\\0\\1\\0\\0\end{bmatrix}+\begin{bmatrix}0\\0\\0\\1\end{bmatrix}$$

A single target is located in range bin 10. Only one PRF with a PRI of 4 range bins is used to make the aliased measurement resulting in a detection in range bin 2. The false alarm adds an additional erroneous detection in range bin 4.

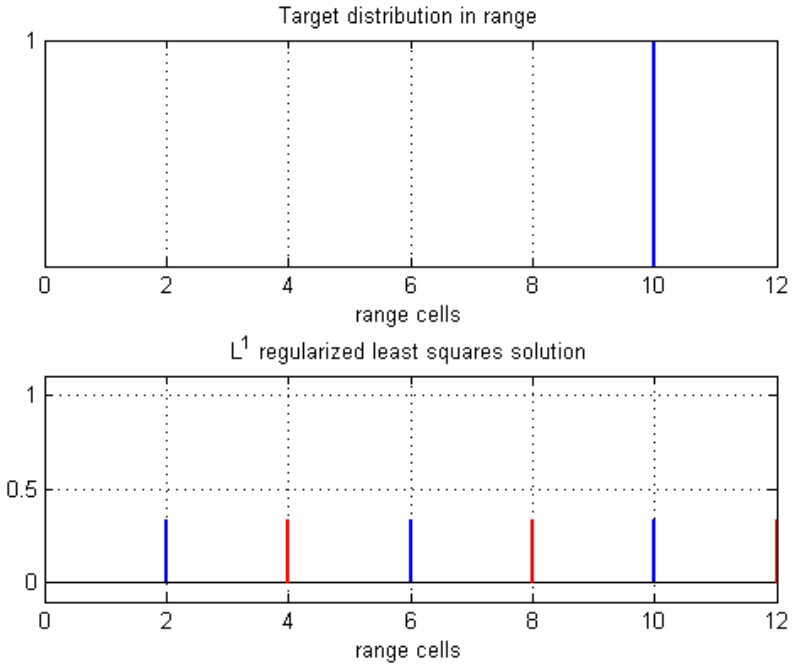

Fig. 5.4 Demonstration of non-zero amplitude locations (in red) due to false alarm with one PRF measurement.

The solution to this system obtained using the L^1 regularized least squares algorithm is shown in Fig. 5.4. Because only 1 PRF was used, the correct detection at aliased bin 2 produces energy at bins 2, 6 and 10, all of which alias to bin 2. All three detections have an amplitude of 1/3. The false alarm at bin 4 similarly produces three candidate detections of amplitude 1/3 at bins 4, 8 and 12.

If we repeat this experiment with two PRFs by adding another PRF with a PRI of 3 range bins in the measurements but with the false alarm only in the first one as before, we get the system shown in Eq. (5.5).

$$\begin{bmatrix} 0 \\ 1 \\ 0 \\ 1 \\ 1 \\ 0 \\ 0 \end{bmatrix} = \begin{bmatrix} 1 & 0 & 0 & 0 & 1 & 0 & 0 & 0 & 1 & 0 & 0 & 0 \\ 0 & 1 & 0 & 0 & 0 & 1 & 0 & 0 & 0 & 1 & 0 & 0 \\ 0 & 0 & 1 & 0 & 0 & 0 & 1 & 0 & 0 & 0 & 1 & 0 \\ 0 & 0 & 0 & 1 & 0 & 0 & 0 & 1 & 0 & 0 & 0 & 1 \\ 1 & 0 & 0 & 1 & 0 & 0 & 1 & 0 & 0 & 1 & 0 & 0 \\ 0 & 1 & 0 & 0 & 1 & 0 & 0 & 1 & 0 & 0 & 1 & 0 \\ 0 & 0 & 1 & 0 & 0 & 1 & 0 & 0 & 1 & 0 & 0 & 1 \end{bmatrix} \begin{bmatrix} 0 \\ 0 \\ 0 \\ 0 \\ 0 \\ 0 \\ 0 \\ 0 \\ 0 \\ 1 \\ 0 \\ 0 \end{bmatrix} + \begin{bmatrix} 0 \\ 0 \\ 0 \\ 1 \\ 0 \\ 0 \\ 0 \end{bmatrix} \quad (5.5)$$

The same target located at range bin 10 in the truth vector **x** now aliases to bins 2 and 5 in the concatenated observation vector **y** on the left hand side of Eq. (5.5). The L^1 regularized least square solution of this two PRF underdetermined system with one false alarm is shown in Fig. 5.5. It is observed that the aliased detections at bins 2 and 5 now produce energy at bins 4 and 10 only in the solution vector which are consistent with *both* the PRF measurements, reducing ambiguity in the target location to two bins. Note that the energy at range bin 10 in the solution vector is the result of actual target detection in the second PRF and the false alarm in the first PRF. This is depicted by two different colors of the line representing the energy at range bin 4. Since there is no error in the second PRF

measurement, adding a consistent measurement reduces the amplitude of the other residuals produced by the false alarm at bins 8 and 12 shown in red.

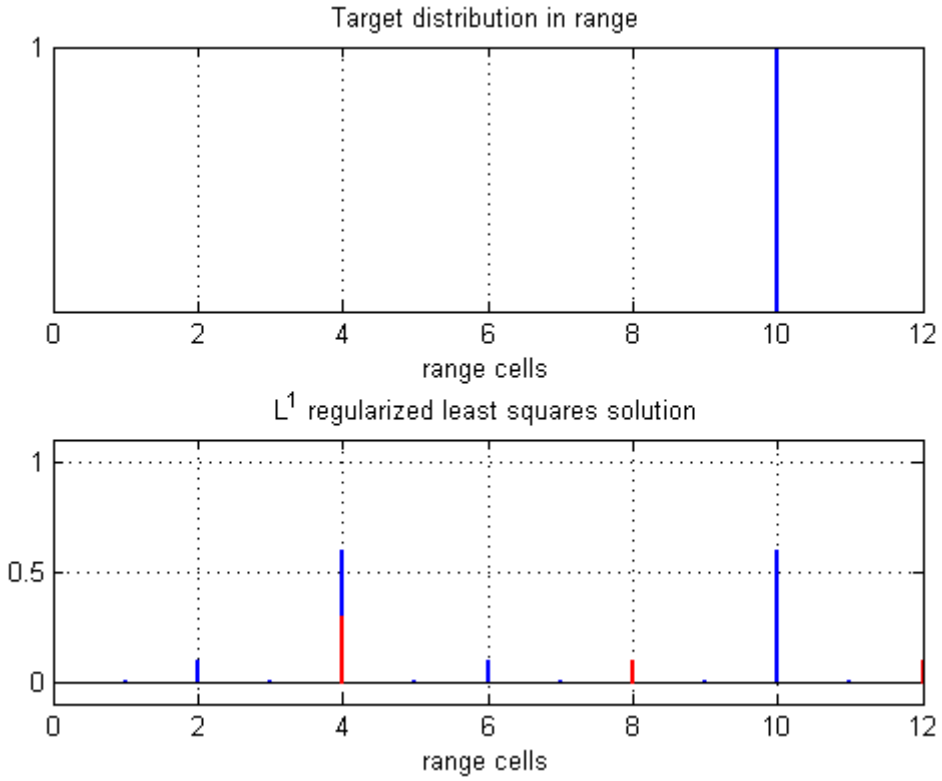

Fig. 5.5 Demonstration of non-zero amplitude locations (in red) due to false alarm with two PRF measurements.

Missed Detections Simulations

Having simulated recovery of disambiguated target locations in the presence of false alarms in the measurements, we now move on to the case of missed detections. Again, using the same three-PRF example with six targets and the truth vector $\mathbf{x} \in \mathcal{B}^{600}$, we will proceed by simulating one missed detection out of a total of 18 detections in the measurements made using three PRFs. This is done by adding a -1 to the observation vector **y** at one of the detected target locations in one of the PRFs. In this example, we simulate missed detection of the target located at range bin number 427 (Fig. 5.1) in the second PRF measurement (PRI=53 μs). This target should alias to range bin number 3 (427 modulo 53) in the measurements made with PRI=53 μs. To simulate the missed detection, we add a -1

to the observation vector at this location. The aliased measurements made with the second PRF are shown in Fig. 5.6 (b), which shows detection of only five of the six targets.

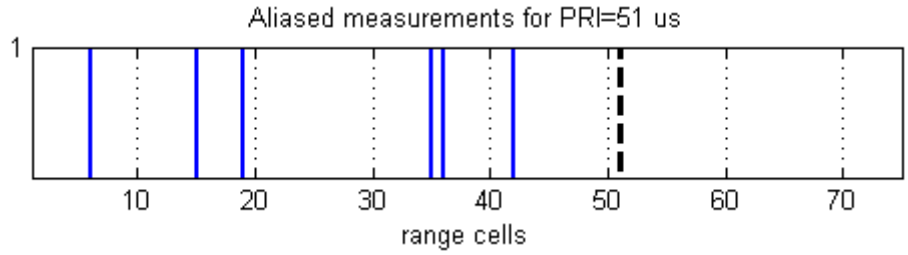

(a)

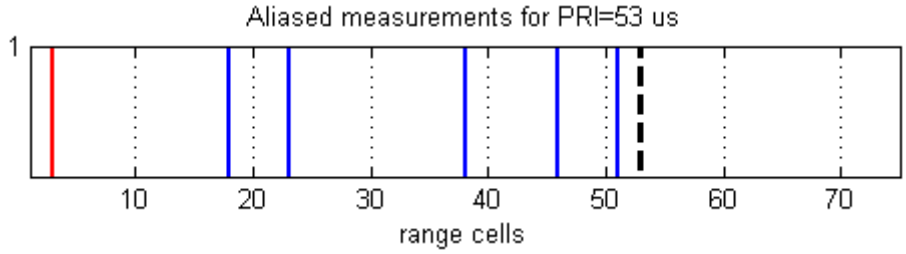

(b)

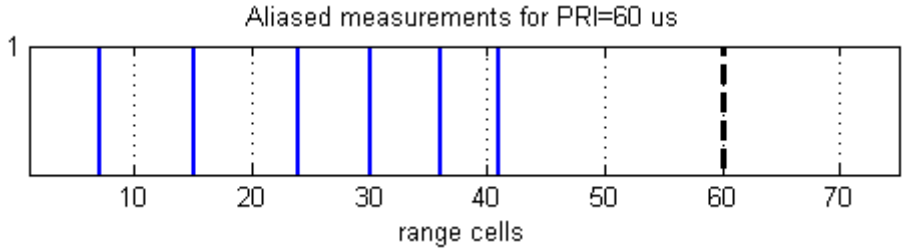

(c)

Fig. 5.6 Multi-PRF aliased measurements with a missed detection. (a) PRI = 51 μs, (b) PRI = 53 μs, missed detection shown in red, and (c) PRI = 60 μs.

The concatenated system of measurements with one missed detection is then solved for the minimum L^1 norm $\mathbf{x}$ with the added constraint of minimum L^1/L^2 residuals. The solutions obtained are shown in Fig. 5.7 (b) and Fig. 5.7 (c). As in the case of false alarms, the targets are resolved in both solutions but the minimum L^2 residuals solution has some energy spread out at other candidate locations in the solution vector for the target at range bin number 427, which arise due to its missed detection in the second PRF measurement.

The average value of the residuals in the minimum L^1 residuals solution is 0.0061, the peak value is 1 (at the missed detection location) and the L^2 norm of the error between the solution vector and truth vector is approximately 1.08×10^{-13}. On the other hand, the average value of residuals in the L^1 regularized least squares solutions is 0.0184, the peak value is 0.2624 and the L^2 norm of the error between the solution vector and truth vector is 0.7872. Multiple trials of the same experiment with different target distributions were conducted and similar results were consistently obtained.

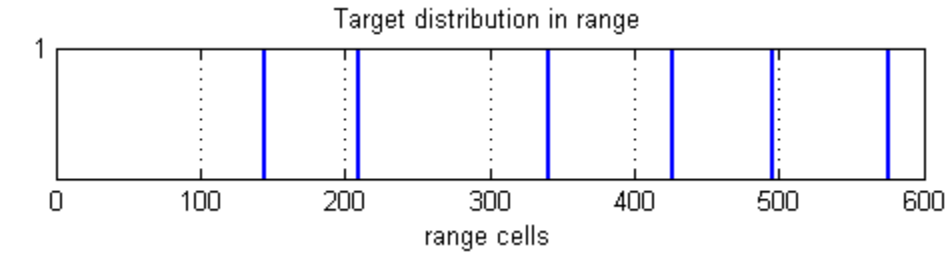

(a)

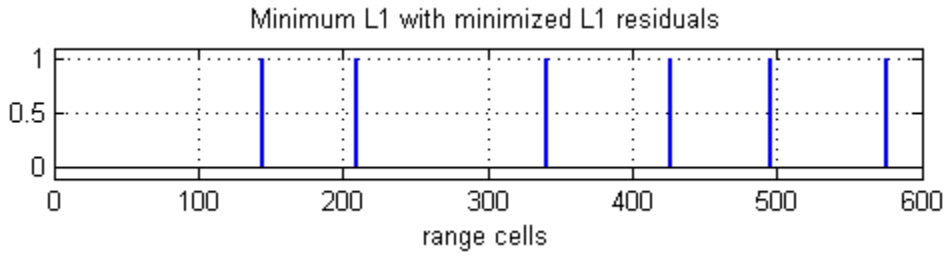

(b)

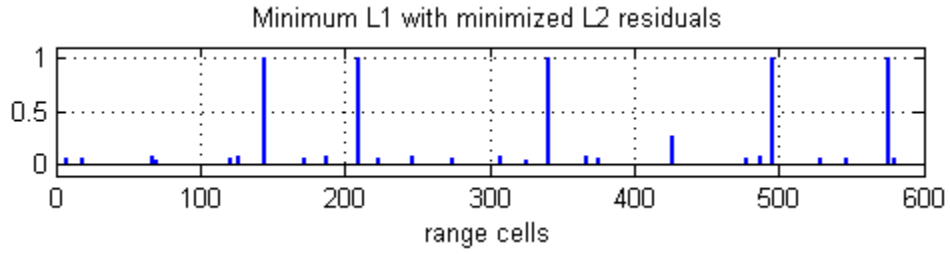

(c)

Fig. 5.7 Comparison of solutions to sample problem with one missed detection. (a) Target distribution, (b) Min L^1 residuals solution and (c) Min L^2 residuals solutions.

Next, using the same example with a different target distribution shown in Fig. 5.8, we set up two more missed detections, one resulting from a collision and one from the target being in the blind zone of one of the PRFs. The blind zones of each PRF in range only, assuming a pulse width of 2 μs, are shown in Fig. 5.9. A target is intentionally placed at range bin number 60, which is in the blind zone of the third PRF, to demonstrate the effect of missed detections due to blind zones.

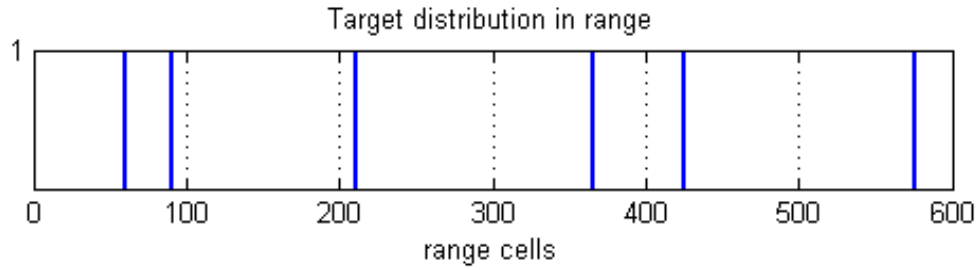

Fig. 5.8 Unaliased target distribution for setting up collisions and blind zone missed detections.

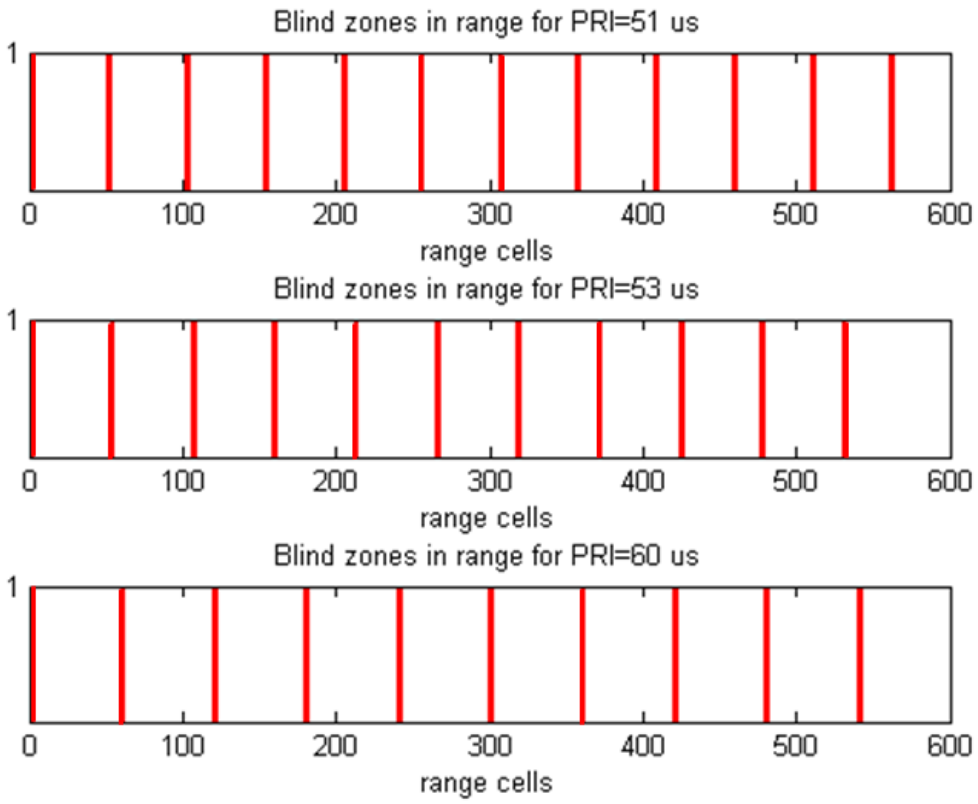

Fig. 5.9 Blind zones in range.

The collision is set up by choosing two of the target locations so that they fold over to the same apparent range bin in one of the PRFs. For the first PRF with PRI=51 μs, the target at range bin number 60 aliases to range bin number 9 (60 modulo 51). The second target is placed at range bin number 366 which also aliases to range bin number 9 (366 modulo 51) for the measurements made with PRI=51 μs. This is illustrated in Fig. 5.10 (a) which shows the observation vectors for each PRF before modeling for collisions and restricting the measurements to binary values only. Fig. 5.11 shows the measurements after the non-binary measurement of targets at range bin number 60 and 366 in the first PRF is changed to a value of 1 to model detection of one target only by adding an error vector with a -1 at the corresponding location.

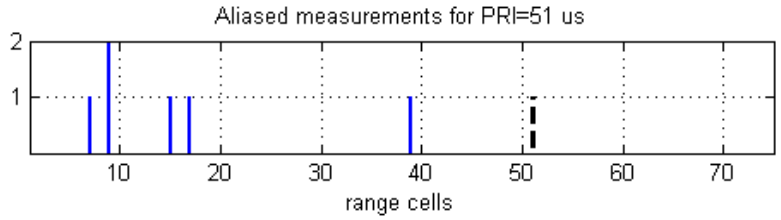

(a)

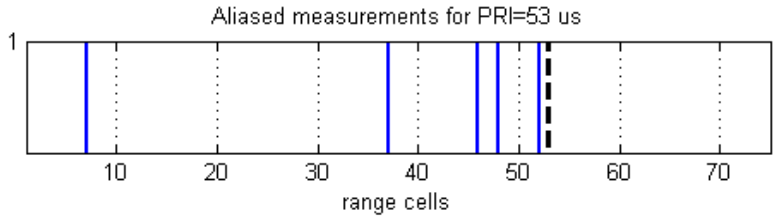

(b)

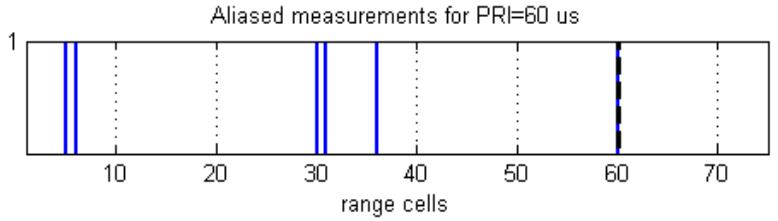

(c)

Fig. 5.10 Multi-PRF aliased measurements with collision. (a) PRI=51 μs, note the non-binary measurement due to collision, (b) PRI=53 μs and (c) PRI=60 μs.

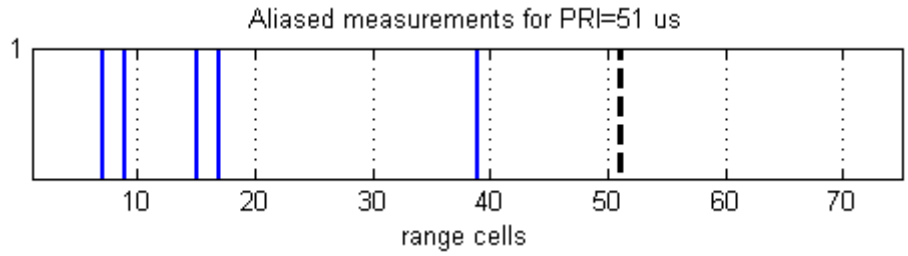

Fig. 5.11 1st PRF measurements clipped to binary values.

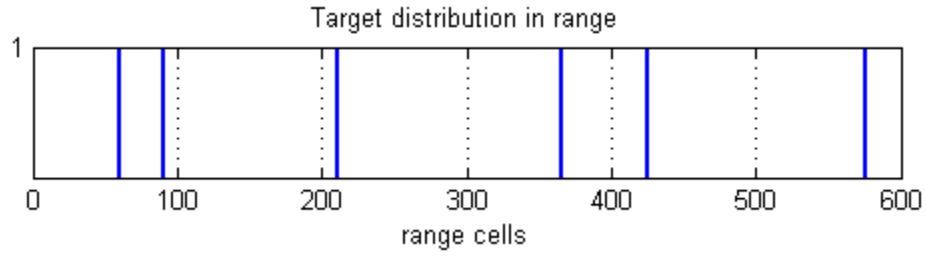

(a)

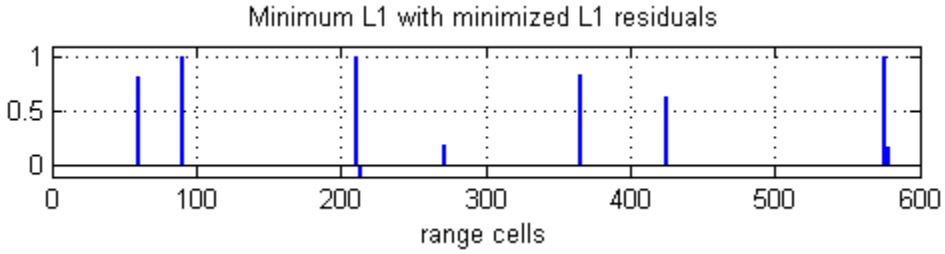

(b)

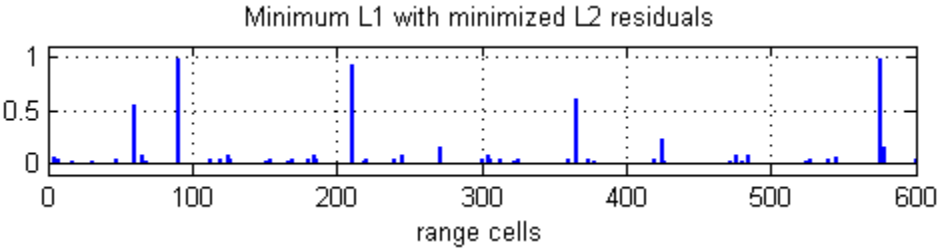

(c)

Fig. 5.12 Comparison of solutions to sample problem with three missed detections. (a) Target distribution, (b) Min L^1 residuals solution and (c) Min L^2 residuals solutions.

The solutions with the minimum L^1/L^2 residuals constraints are shown in Fig. 5.12 (b) and (c). We see that with the addition of more errors in the measurements in the form

of missed detections, the recovery is not exact and some of the targets have their energies spread in more than one range bin in both solutions. However, the minimum L^1 residuals solutions is still seen to be sparser than the minimum L^2 residuals solution.

Multiple trials of this simulation with the same number of errors but different target distributions produced similar results. It was noted earlier that the number of measurements on the order of ($k \cdot \log_2 n$) are required to solve the basis pursuit problems in the absence of errors as shown in Fig. 4.8 and Fig. 4.9. For this simulation, $k \cdot \log_2 n = 6 \cdot \log_2(600) \approx 55$ measurements. However, our experimental results in the case of basis pursuit denoising suggest that a greater number of measurements would be required to solve the problem in the presence of measurement errors in the system. The total number of measurements m_s in this simulation is 51+53+60=164 which gives an m_s/n ratio of approximately 0.27. One of the reasons for using this PRF set with greater number of measurements is to minimize the common blind zones of the three PRFs in the range space.

We will now attempt to solve the system with an additional set of measurements carried out with PRI=63 μs, which is next in the set of eight PRIs in [28] selected using evolutionary algorithms. The aliased measurements made with the four PRFs are shown in Fig. 5.13, and the solutions obtained from these measurements are shown in Fig. 5.14 (b) and (c). The minimum L^1 residuals solution now shows exact recovery of the truth vector **x**. The L^1 regularized least squares solution still has degraded amplitudes for some targets but these amplitudes are significantly higher than the unwanted residual signals in the solution vector. This and other similar experiments conducted during the course of this research show that depending on the number of errors in the system, increasing the number of measurements by adding more PRFs in the measurement structure ultimately results in the successful recovery of all the targets in the solution vector. This is consistent with the results obtained in Fig. 4.9 for the recovery in the absence of noise.

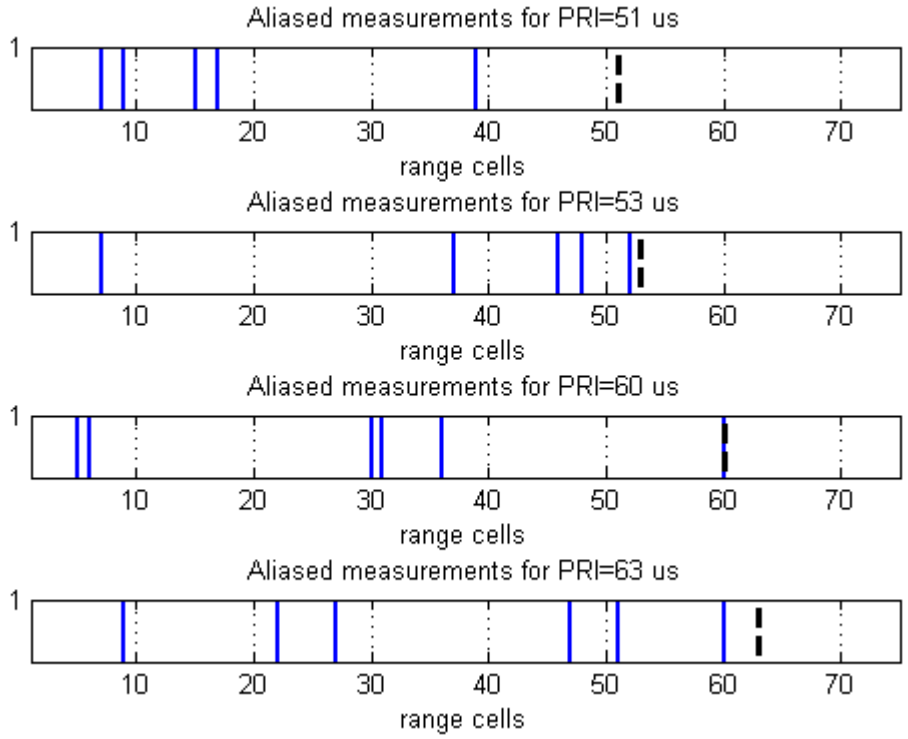

Fig. 5.13 Multi-PRF aliased measurements with an extra PRF.

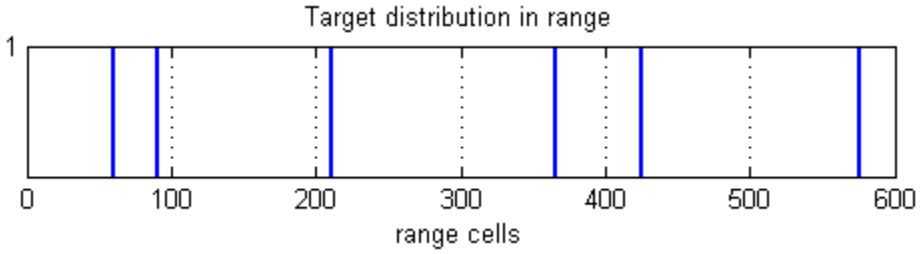

(a)

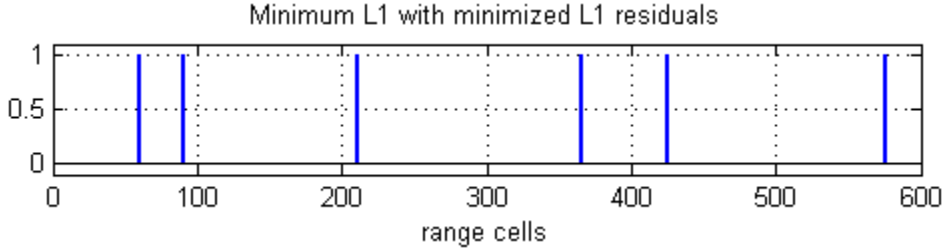

(b)

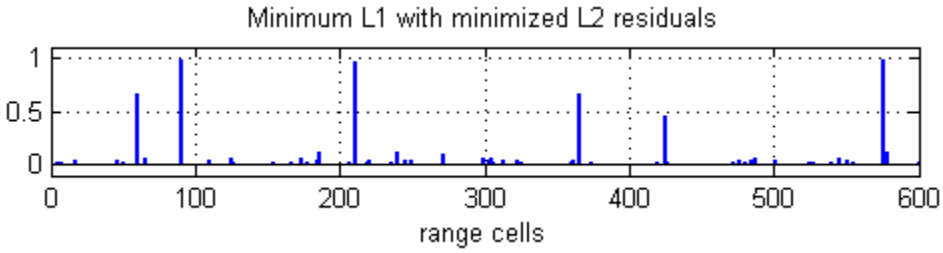

(c)

Fig. 5.14 Comparison of solutions to the multiple missed detections problem using an extra PRF. (a) Target distribution, (b) Min L^1 residuals and (c) Min L^2 residuals solution.

A "Real World" Example

So far, we have given examples showing the effects of errors in the measurements but only taking into account a few sources of error at a time, and for the one dimensional case of range ambiguities only. We will now consider the two dimensional range-Doppler ambiguities and simulate the new ambiguity resolution technique taking into account *all* the real world effects with realistic error probabilities.

The same radar parameters used for the range-Doppler example in Chapter 4, based on the X-band airborne pulse Doppler medium PRF radar [28], will be used for this simulation. Twenty targets are randomly distributed in the range-Doppler matrix consisting of 200,000 range-Doppler bins, and aliased measurements are made with the eight PRFs from the medium PRF set obtained using evolutionary algorithms. False alarms are added to each measurement at random locations in the observation vector assuming $P_{FA}=10^{-4}$, i.e. 1 per 10,000 detections, or 20 false alarms in each set of measurements. Missed detections are simulated assuming $P_D=0.9$. They are implemented by generating a uniform random variable vector in each PRF containing pseudorandom values drawn from the standard uniform distribution on the open interval (0,1) for each target using the Matlab *rand* function. The random vector is of the same size as the target sparsity and each target is associated with the corresponding probability value from the uniform distribution. Targets with an associated random variable greater than 0.1 are passed as "detected" targets, while

those with the random variable less than 0.1 are considered as missed detections and removed from the assumed target distribution in the range-Doppler matrix. The collisions, if any, are clipped to a value of 1 in the observation vector allowing for the detection of one target only. Finally, the blind zones of all PRFs in the 8-PRF set are determined and any targets which happen to be in the blind zone for a given PRF are simulated as undetected. There are many more blind cells in the two dimensional range-Doppler case than in the range-only case considered earlier. Consider PRI=51 μs as an example, assuming 10 blind range cells and 17 blind velocity cells [28] in each pulse repetition interval, the total number of blind cells in range-only case will be 39,220 assuming n=200,000 range cells. On the other hand, the total number of blind cells in the range-Doppler case are 136,371 assuming n=200,000 range-Doppler cells. This is because the blind zones in range have to be extended in the Doppler dimension, and the blind zones in Doppler get extended in the range dimension. This is shown in Fig. 5.15 (a), (b) and (c) for the first three PRFs of the set.

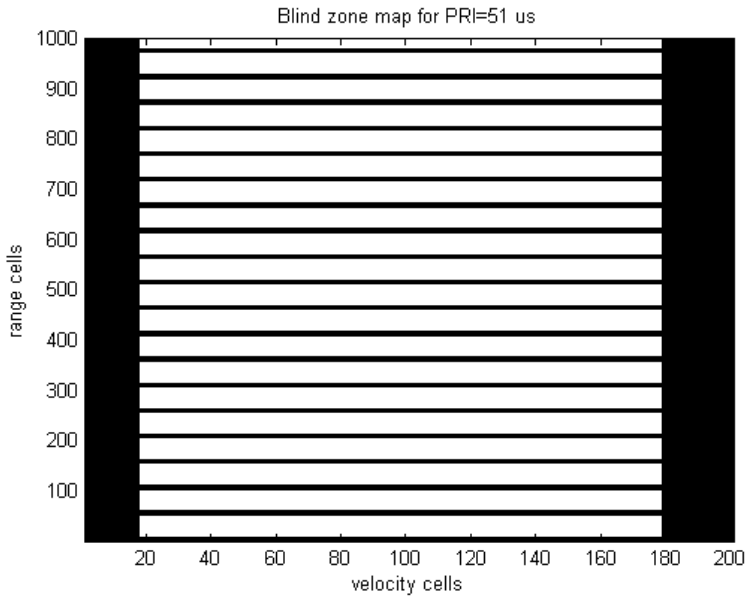

(a)

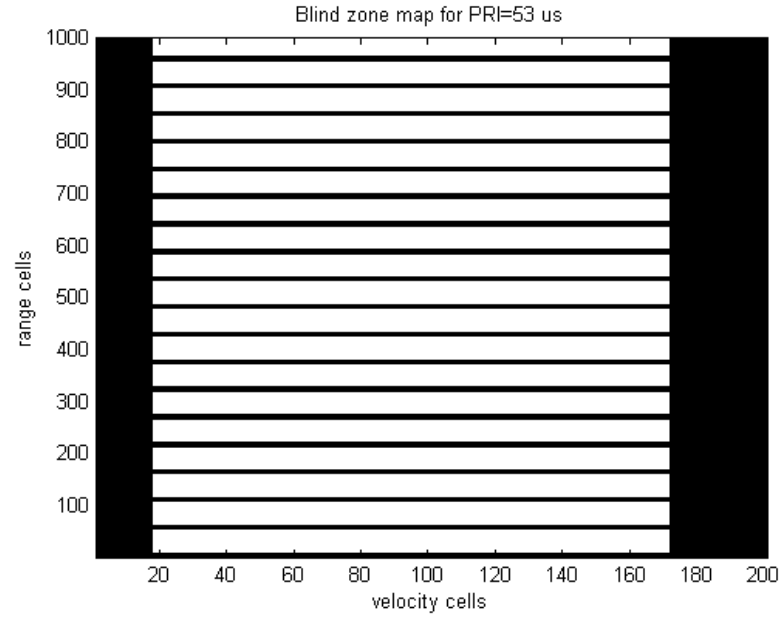

(b)

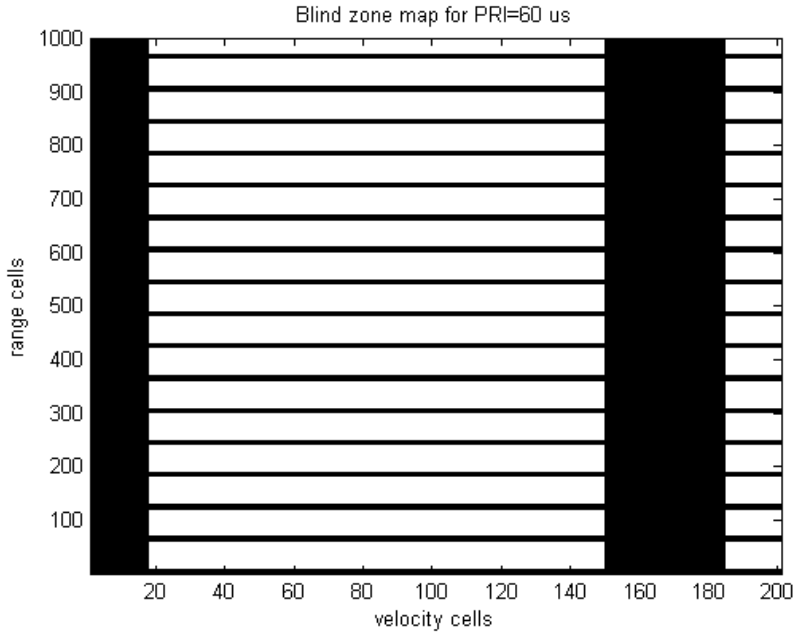

(c)

Fig. 5.15 Blind zone maps of the first three PRFs in the 8-PRF set.
(a) PRI=51 μs, (b) PRI=53 μs and (c) PRI=60 μs.

It can be seen that the exact locations of the blind regions are PRF dependent, except for the first eclipsed range along the bottom of the map and the first case of main lobe

clutter rejection along the left hand edge of the map, which remains fixed in all PRFs. In any single PRF there is a significant probability that a target will go undetected because of the blindness inherent in the PRF [3]. Therefore, the problem is to select a set of PRFs such that all ranges and Doppler frequencies that the radar must cover fall in a clear region for at least the several PRFs that are needed to resolve the ambiguities in range and Doppler. In conventional practice, three or more PRFs are required to be clear for any one target to achieve satisfactory detection probabilities and ranges [28]. As we will see later, detection in three or more PRFs is also sufficient for our new L^1 minimization technique to successfully disambiguate the aliased measurements. The 8-PRF set selected using evolutionary algorithm ensures that most of the areas of the range-Doppler space are covered by at least three PRFs to detect the target reliably. This is illustrated in Fig. 5.16 which shows the 3 of 8 detection map of the 8-PRF set. The white areas represent the space where the target could be detected in three or more of the eight PRFs, while the black streaks represent the bins where a target will be detected in less than three PRFs.

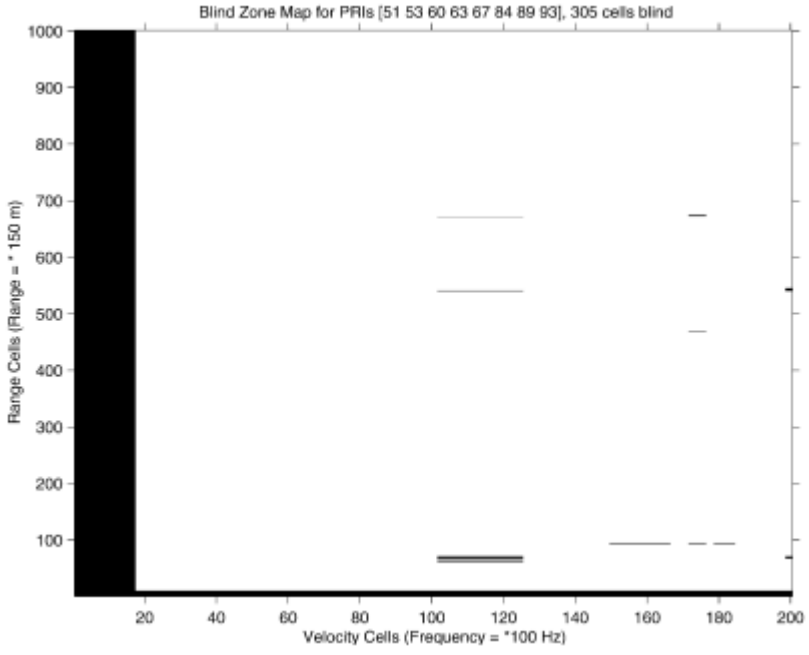

Fig. 5.16 3 of 8 blind zone map for 8 PRFs found by evolution [28].

We attempted solving this problem with the usual approach of minimum L^1 with minimized L^2 and L^1 residuals. The Matlab implementation of the minimum L^2 residuals solution *l1_ls* [32] is optimized to solve large sparse problems efficiently. As a result, the L^1 regularized least squares solution was obtained in a few seconds using this solver on a standard laptop computer. However, the CVX implementation of the minimum L^1 residuals solution required extra memory and special computer equipment had to be arranged. Figure 5.17 (a) shows the random target distribution in range-Doppler space in vector form, and the vectorized L^1 recovery with minimum L^1 and minimum L^2 residuals is shown in Fig. 5.17 (b) and 5.17 (c) respectively. The minimum L^1 residuals solution is again seen to be sparser than the L^1 regularized least squares solution with no unwanted residuals. However, only the targets detected in more than 4 of the 8 PRFs are recovered (see Table 5.1 for target locations and their detections in individual PRFs). This is because the algorithm identifies the detections in a few of the total number of PRFs as erroneous measurements and suppresses them in the solution. The L^1 regularized least squares solution has unwanted residuals in the solution vector but it recovers all the targets in the solution vector albeit with different amplitudes. It is observed that the target energy in the solution vector depends on the number of PRFs in which it is detected.

Table 5.1 gives the target position in the range-Doppler space, the specific PRFs in which each target is detected, and the amplitude of the target in the L^1 regularized least squares solution vector. It can be seen that the target amplitudes are, in general, approximately proportional to the number of PRFs in which they are detected, and distinguishable from the residual errors in the solution vector as shown in Fig. 5.17 (c). This shows that an ambiguity resolution algorithm can be based on minimizing the L^1 norm of $\mathbf{x}$ under the constraint of minimizing the L^1/L^2 norm of the residuals followed by appropriate thresholding and provided the target is detected in a sufficient number of PRFs.

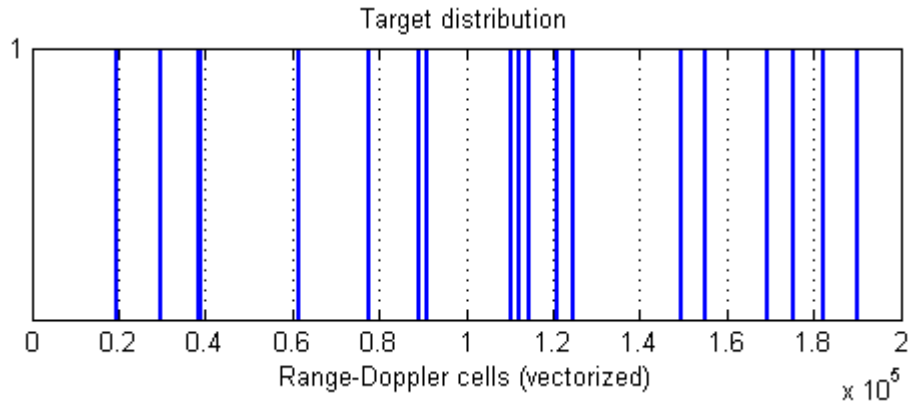

(a)

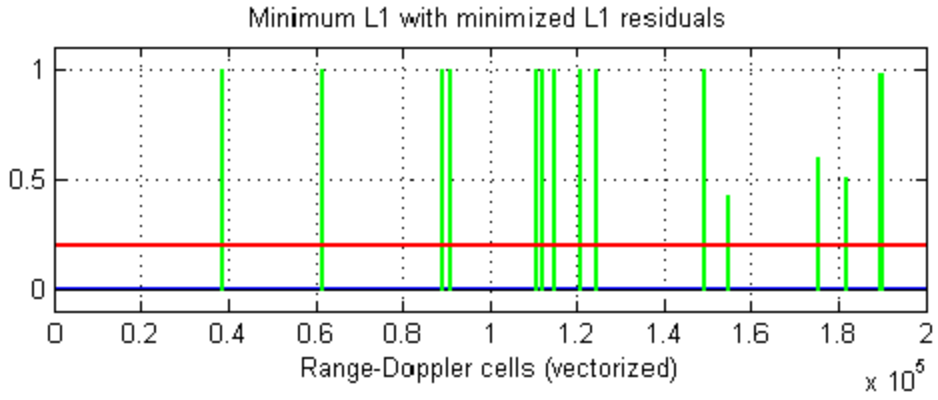

(b)

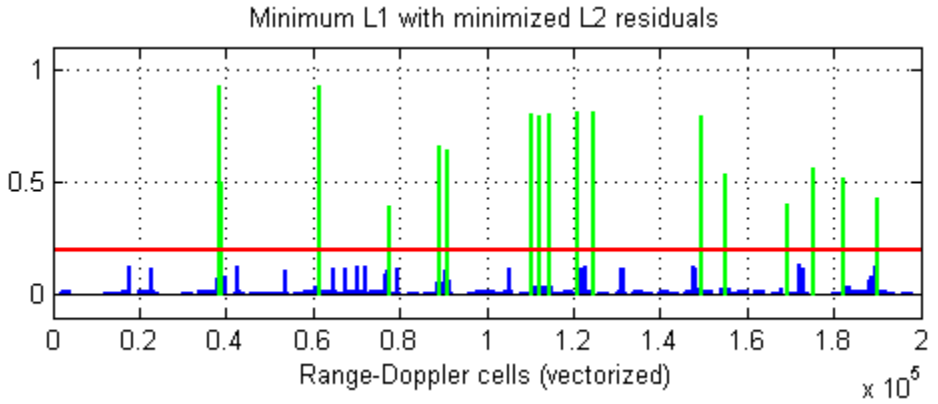

(c)

Fig. 5.17 Comparison of solution to the real world example.
(a) Original target distribution and (b) Min L^1 residuals solution in vector form, and (c) Min L^2 residuals solution in vector form

TABLE 5.1 Target amplitude variation with number of detections.

Target position (Cell#)	Detections								Amplitude in the solution vector	Amplitude normalized over the number of detections
	PRF1	PRF2	PRF3	PRF4	PRF5	PRF6	PRF7	PRF8		
19356									0.0000	0.0000
29828									0.0000	0.0000
38551	✓	✓	✓	✓	✓	✓	✓	✓	0.9084	0.1135
39077	✓	✓	✓			✓		✓	0.3622	0.0724
61297	✓	✓	✓	✓	✓	✓	✓	✓	0.9375	0.1171
77681	✓	✓		✓			✓		0.3957	0.0989
89176			✓	✓	✓	✓	✓	✓	0.6480	0.1080
90928		✓	✓	✓	✓		✓	✓	0.8091	0.1348
110288	✓	✓	✓	✓	✓	✓	✓		0.7923	0.1131
112088	✓	✓	✓	✓	✓		✓	✓	0.8016	0.1145
114597	✓	✓	✓	✓	✓		✓	✓	0.7985	0.1140
120979		✓	✓	✓	✓	✓	✓	✓	0.9375	0.1339
124584			✓	✓	✓	✓	✓	✓	0.7966	0.1327
149312	✓	✓	✓	✓	✓	✓	✓		0.8091	0.1348
155080		✓	✓			✓	✓	✓	0.5343	0.1068
169433			✓	✓	✓			✓	0.4027	0.1006
175429		✓	✓	✓	✓			✓	0.5529	0.1105
182135	✓	✓	✓			✓	✓		0.5122	0.1024
189951	✓	✓	✓	✓		✓			0.4640	0.0928
190261		✓	✓		✓				0.2457	0.0819

Further trials of this simulation with different target distributions showed that target detection in three or more PRFs consistently produces target amplitudes significantly higher than those of residual errors in the solution vector, which enables target recovery in the solution vector. Experimental results also showed that the residual errors in the solution

vector due to errors in the measurement can be rejected by setting a threshold at amplitude=0.2. This is indicated by red line in Fig. 5.17 (c). The solution in two-dimensional range-Doppler space after setting the threshold at 0.2 is shown in Fig. 5.18 which shows disambiguated recovery of all targets but two (cell numbers 19356 and 29828 in Table 5.1) at range-Doppler coordinates (10, 1356) and (15, 1828) that happen to be in the blind region of all eight PRFs.

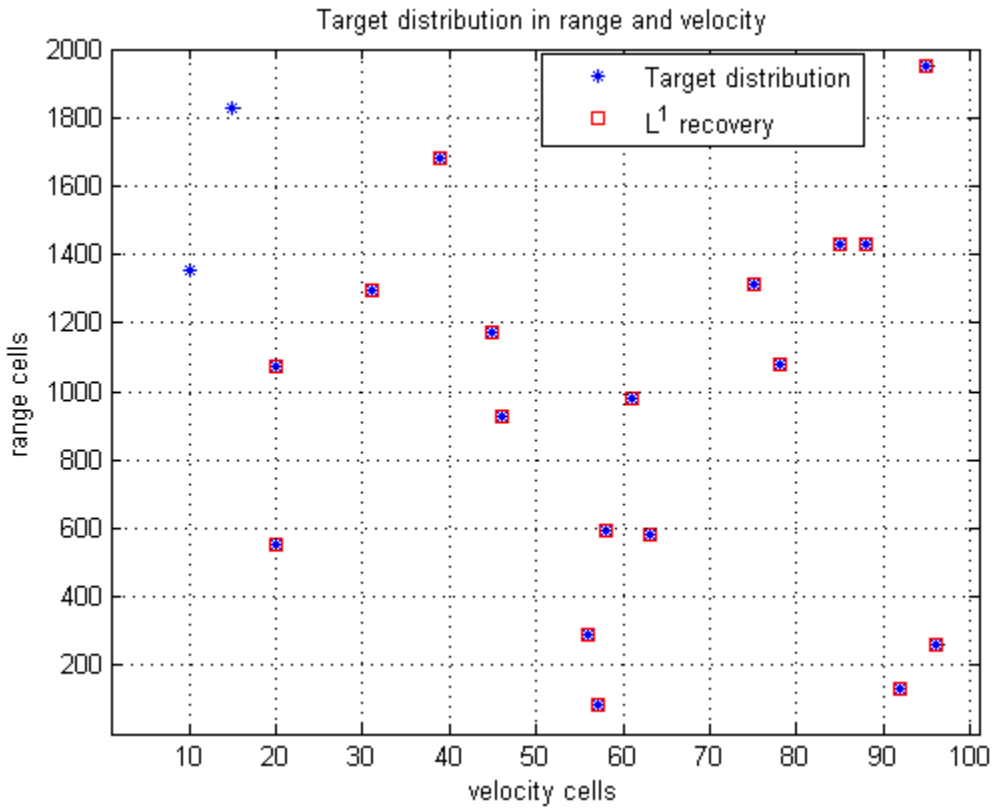

Fig. 5.18 Target distribution and Min L^2 residuals solution in Range-Doppler.

CHAPTER 6

CONCLUSION

In this chapter, we will summarize and conclude the discussion presented in chapters 1-5. We started off with a literature review of the measurement process in pulse Doppler radars to understand the measurement of range and Doppler through transmission of a periodic series of pulses and the subsequent fast-time/slow-time sampling of the return signals. The resulting measurements are aliased in both range and Doppler in medium PRF radars giving rise to range and Doppler ambiguities. This problem is addressed by repeating the measurements with several different PRFs producing different aliasing characteristics. One of several ambiguity resolution algorithms is then applied to the combined measurements to determine the true unaliased range-Doppler pairs.

The current algorithms for ambiguity resolution are based primarily on the Chinese remainder theorem and extensions of the basic CRT scheme. They require at least (k+1) PRFs to resolve k targets. Further study of the CRT-based algorithms revealed that they require a very particular set of PRFs for ambiguity resolution. These techniques may also require one set of PRFs to resolve range ambiguities and another set for Doppler ambiguities. Furthermore, the CRT algorithm is inherently very sensitive to errors in the measurement and detection process. Most of the ambiguity resolution algorithms proposed in radar literature are an improved extension of the basic CRT scheme. In this research, we propose a novel L^1 minimization based approach for range-Doppler ambiguity resolution in pulse Doppler radars inspired by the applications of compressed sensing for sparse signal recovery. To investigate the usefulness of this technique in the ambiguity resolution process, we first needed to develop a sparse representation of the measurement structure and detection results in pulse Doppler radars.

The radar detection process involves making decisions about the presence or absence of a target in each cell based on the range and Doppler measurements degraded with noise and interference. The outcome of this statistical hypothesis testing process is binary, i.e. target present or not present. It was also observed that the target detections exist in only a few range/velocity cells. Therefore, we could represent the post-detection data as a sparse binary vector. To represent the measurements made with individual PRFs, we constructed binary Toeplitz matrices with ones representing the transmission of pulses and the interval between the pulses represented by the zeros equal in number to the range cells in a given PRI. Representing the measurements and the post-detection data in this manner allowed us to model the ambiguity resolution problem as a linear system of equations. In most situations of interest, this system is underdetermined.

Since a consistent underdetermined system of equations has infinitely many solutions, the problem then was to find a way to determine a sparse solution to the system that would give the correct unaliased detection map in range and Doppler. In other words, we sought to find the minimum L^0 solution to the system, a problem known to be Np-hard. However, it was determined from the compressed sensing literature that the minimum L^1 solution is also the sparsest solution to many underdetermined systems and that the L^1/L^0 equivalence holds when the solution to the system is sufficiently sparse. It was also determined that under certain conditions, which are satisfied by our mathematical model of the post-detection data in pulse Doppler radars, the condition for the successful L^1 recovery of the sparse vector reduces to simply the condition of there being a unique vector in the constraint set. The mathematical model was first developed to account for range measurements and ambiguities only, and then extended in another dimension to account for Doppler ambiguities as well. The compressed sensing literature research on the minimum number of measurements required for L^1 recovery showed that $O(k \cdot \log_2 n)$ measurements required for partial Fourier matrices are, in practice, also sufficient for binary and sparse measurement matrices.

After completing the background research and developing the mathematical model for the idealized case with no errors in the measurement and detection process, we proceeded to simulate the ambiguity resolution process using L^1 minimization. The Matlab-based CVX package was used for L^1 minimization and a range-only simulation was first carried out as a proof-of-concept demonstration. It was observed that the new technique worked well and the recovery was exact in the idealized case. Simulations were then carried out for the two-dimensional range-Doppler case and the ambiguities were again successfully resolved in both range and Doppler. To investigate the effects of changing the number of measurements and the target sparsity as predicted by the relation for the required number of measurements for sparse recovery, we carried out multiple trials of the simulation with different values of these parameters. Empirical results confirmed that the L^1 recovery was successful with the number of measurements given by $O(k \cdot \log_2 n)$. Furthermore, it was also observed that in addition to the target sparsity and the problem dimension, the required number of measurements also depends on the number of PRFs used to obtain the measurements and that the unambiguous vector could be recovered with fewer number of measurements if the number of PRFs was increased.

Once a basic ambiguity resolution capability was developed using L^1 minimization for the idealized case, the behavior of this technique was investigated in the presence of real-world effects like false alarms and missed detections, as well as missed detections due to blind zones and collisions in the multi-PRF radar measurements. We showed that the false alarms and missed detections can be modeled by adding an error vector to the system which takes on the values of +1 for false alarms and -1 for missed detections at the corresponding target locations. It was shown that the blind zone effects and collisions can also be modeled as missed detections in the same way. The resulting basis pursuit denoising problem was solved using two approaches, both solving for the minimum L^1 norm solution vector but under different constraints with respect to minimizing the residual error. The minimum L^2 residuals solution was obtained using the L^1 regularized least squares method

implemented with the help of a Matlab-based solver *l1_ls* expressly developed to solve large problems in basis pursuit denoising. The minimum L^1 residuals solution was obtained using the CVX package. Empirical results showed that the targets could be successfully resolved using both approaches in the presence of errors but a greater number of measurements was required than in the idealized case, and the required number of measurements increased with the number of errors in the system. It was also observed that the solution obtained using the latter approach was sparser than the L^1 regularized least squares solution and did not have the unwanted residual elements in the solution vector. However, the minimum L^1 residuals solution in the range-Doppler case failed to recover targets detected in only a few of the total number of PRFs as they could not be distinguished by the algorithm from the measurement errors. The L^1 regularized least squares solution recovered all the targets with their amplitudes in the solution vector approximately proportional to the number of detections in the individual PRFs. It was shown that the unwanted residuals in the solution vector could be rejected by appropriate thresholding.

In conclusion, the research showed that the L^1 minimization methods can be successfully implemented for range-Doppler ambiguity resolution in pulse Doppler radars. The behavior of the technique was characterized in terms of the required number of measurements, the number of PRFs used and the target sparsity in the idealized case with no errors. The technique was also seen to work well in the presence of real world effects and several examples were provided to this end. Future research will focus on the characterization of the new technique in terms of the number of measurements required and the number of errors in the system. In addition, an analytical approach for determining the threshold to reject the unwanted residuals in the solution vector in the presence of errors is also an interesting topic for future research.

REFERENCES

[1] M. A. Richards, *Fundamentals of Radar Signal Processing*. New York: McGraw-Hill, 2005.

[2] M. A. Richards, J. A. Scheer, and W. A. Holm, editors, *Principles of Modern Radar: Basic Principles*, SciTech Publishing, 2010.

[3] C. Alabaster, *Pulse Doppler Radar: Principles, Technology, Applications*, SciTech Publishing, 2012.

[4] H. Meikle, *Modern Radar Systems*, Artech House, 2008.

[5] A. G. Thomas and M.C. Berg, *Medium PRF set selection: An approach through combinatorics,* IEE Proceedings – Radar, Sonar Navigation, Dec 1994, 307-311.

[6] A. Ferrari, C. Béranguer, and G. Alengrin, *Doppler ambiguity resolution using multiple PRF,* IEEE Trans. Aerosp. Electron. System, pp. 738–751, Jul. 1997.

[7] W. Lei, T. Long, W. Han, *Resolution of Range and Velocity Ambiguity for a Medium Pulse Doppler Radar*, Record of the IEEE 2000 International Radar Conference, IEEE AESS, 2000.

[8] D. Needell, *Noisy signal recovery via iterative reweighted L^1-minimization*. In Proc. 43rd Ann. Asilomar Conf. Signals, Systems, and Computers, 2009.

[9] D.L. Donoho, *For most large underdetermined systems of linear equations the minimal l1-norm solution is also the sparsest solution*. Comm. Pure Appl. Math. 59 (2006), 797–829.

[10] D.L. Donoho and X. Huo, *Uncertainty principles and ideal atomic decomposition*, IEEE Transactions on Information Theory, 47 (2001), 2845–2862.

[11] J. Tanner and D. Donoho. *Thresholds for the Recovery of Sparse Solutions via L^1 Minimization*, Proceedings of the Conference on Information Sciences and Systems, March 2006.

[12] Y. Tsaig and D.L. Donoho, *Breakdown of equivalence between the minimal L^1 norm solution and the sparsest solution*. EURASIP Journal of Applied Signal Processing, 2005.

[13] E. Candès, J. Romberg, and T. Tao, *Robust uncertainty principles: Exact signal reconstruction from highly incomplete frequency information*, IEEE Trans. Inform. Theory, vol. 52, no. 2, pp. 489–509, Feb. 2006.

[14] E. J. Candès and M. B. Wakin, *An introduction to compressive sampling*, IEEE Signal Processing Magazine, vol. 21, no. 3, pp. 21–30, 2008.

[15] E. Candès and J. Romberg, *Sparsity and incoherence in compressive sampling*, Inverse Prob., vol. 23, no. 3, pp. 969–985, 2007.

[16] V. Chandar. *A negative result concerning explicit matrices with the restricted isometry property*, Technical report, 2008, available online at http://dsp.rice.edu/files/cs/Venkat_CS.pdf.

[17] R. Berinde, A. Gilbert, P. Indyk, H. Karloff, and M. Strauss, *Combining geometry and combinatorics: a unified approach to sparse signal recovery*, 46th Annual Allerton Conference on Communication, Control, and Computing, pp. 798-805, September 2008.

[18] A. Khajehnejad, W. Xu, A. Dimakis and B. Hassibi, *Sparse Recovery of Nonnegative Signals with Minimal Expansion*, IEEE Transactions on Signal Processing, 2010, Vol. 59(1), pp. 196-208.

[19] A. Khajehnejad, A. S. Tehrani, A. G. Dimakis, and B. Hassibi, *Explicit matrices for sparse approximation*, IEEE Int. Symp. Inf. Theory, Jul. 31–Aug. 5 2011, pp. 469–473.

[20] R. Berinde and P. Indyk. *Sparse recovery using sparse random matrices*, MIT-CSAIL Technical Report, 2008, available online at http://people.csail.mit.edu/indyk/report.pdf.

[21] S. Chen, D. Donoho, and M. Saunders. *Atomic decomposition by basis pursuit*, *SIAM J. Sci Comp.*, 20(1):33–61, 1999.

[22] I. Loris, *On the performance of algorithms for the minimization of L^1 penalized functionals*, Inverse Problems, vol. 25, pp. 1–16, 2009.

[23] S. Becker, J. Bobin, and E. Candès, *NESTA: a fast and accurate first order method for sparse recovery*, Technical report, California Institute of Technology, 2009.

[24] M. Zibulevskyb and M. Elad, *L^1-L^2 optimization in signal and image processing*, IEEE Signal Processing Magazine, vol. 27, no. 3, pp. 76 – 88, 2010.

[25] CVX Research, Inc. CVX: Matlab software for disciplined convex programming, version 2.0 beta.http://cvxr.com/cvx, September 2012.

[26] M. Grant and S. Boyd. *Graph implementations for nonsmooth convex programs, Recent Advances in Learning and Control (a tribute to M. Vidyasagar)*, V. Blondel, S. Boyd, and H. Kimura, editors, pp. 95-110, Lecture Notes in Control and Information Sciences, Springer, 2008. http://stanford.edu/~boyd/graph_dcp.html.

[27] T. A. Davis. *Direct Methods for Sparse Linear Systems*, Fundamentals of Algorithms. *SIAM*, 2006.

[28] Davies, P. G., and Hughes, E. J. *Medium PRF set selection using evolutionary algorithms*, IEEE Transactions on Aerospace and Electronic Systems, 38, 3 (July 2002), 933—939.

[29] E. J. Hughes and C. M. Alabaster, *Novel PRF Schedules for medium PRF radar*, In Proceedings of the Radar 2003 Conference, Adelaide, S. Australia, September 2003.

[30] M. Schmidt, G. Fung, and R. Rosales, *Optimization methods for L^1-regularization*, University of British Columbia, Technical Report TR-2009-19, 2009.

[31] S.J. Kim, K. Koh, M. Lustig, S. Boyd, and D. Gorinevsky, *An interior point method for large-scale L^1-regularized least squares*, IEEE Journal on Selected Topics in Signal Processing, vol. 1, no. 4, pp. 606–617, December 2007.

[32] K. Koh, S. J. Kim, S. Boyd, available online at http://www.stanford.edu/~boyd/l1_ls/

[33] T. Terlaky, *Interior Point methods in Mathematical Programming*, Kluwer, 1996.